Ore Geology Reviews 84 (2017) 347–363

Contents lists available at ScienceDirect

Ore Geology Reviews

journal homepage: www.elsevier.com/locate/oregeo

Two pulses of mineralization and genesis of the Zhaxikang Sb–Pb–Zn–Ag deposit in southern Tibet: Constraints from Fe–Zn isotopes

Da Wang [a], Xiang Sun [a,*], Youye Zheng [a,b,*], Song Wu [a], Shenlan Xia [a], Huifang Chang [a], Miao Yu [c]

[a] State Key Laboratory of Geological Processes and Mineral Resources, School of Earth Sciences and Mineral Resources, China University of Geosciences, Beijing 100083, China
[b] State Key Laboratory of Geological Processes and Mineral Resources, China University of Geosciences, Wuhan 430074, China
[c] Beijing Institute of Geology, Beijing 100120, China

ARTICLE INFO

Article history:
Received 27 February 2016
Received in revised form 28 December 2016
Accepted 30 December 2016
Available online 12 January 2017

Keywords:
Zhaxikang deposit
Fe–Zn isotopes
Two pulses of mineralization
Genesis
North Himalaya

ABSTRACT

Zhaxikang is one large Sb–Pb–Zn–Ag deposit located in the North Himalaya of southern Tibet. To date, the genesis of this deposit still remains controversial. Here, we present new pyrite Fe and sphalerite Zn isotopic data for the first three stages of mineralization, Fe–Zn isotopic data for Mn–Fe carbonate that formed during the first two stages of mineralization, and Zn isotopic data for the slate wall rocks of the Jurassic Ridang Formation to discuss the genesis of the Zhaxikang deposit. The overall δ^{56}Fe and δ^{66}Zn values range from −0.80‰ to 0.43‰ and from −0.03‰ to 0.38‰, respectively. The δ^{56}Fe values of Mn–Fe carbonates are lighter than those of associated pyrite in six mineral pairs, indicating that the iron carbonates are preferentially enriched in light Fe isotopes relative to pyrite. The sphalerite has lighter δ^{66}Zn values than associated Mn–Fe carbonates in three mineral pairs.

The δ^{56}Fe values of pyrite that formed during the first three stages of mineralization gradually increase from stage 1 (−0.33‰ to −0.09‰) through stage 2 (−0.30‰ to 0.19‰) to stage 3 (0.16‰–0.43‰). In comparison, the sphalerite that formed during these stages has δ^{66}Zn values that gradually decrease from stage 1 (0.16‰–0.35‰) through stage 2 (0.09‰–0.23‰) to stage 3 (−0.03‰ to 0.22‰). These data, in conjunction with the observations of hand specimens and thin sections, suggest that the deposit was overprinted by a second pulse of mineralization. This overprint would account for these Fe–Zn isotopic variations as well as the kinetic Rayleigh fractionation that occurred during mineralization. The temporally increasing δ^{56}Fe and decreasing δ^{66}Zn values recorded in the deposit are also coincident with an increase in alteration, again supporting the existence of two pulses of mineralization. The δ^{56}Fe values of the first pulse of ore-forming fluid were calculated using theoretical equations, yielding values of −0.54‰ to −0.34‰ that overlap with those of submarine hydrothermal solutions (−1‰ to 0‰). However, the δ^{56}Fe values of the stage 3 pyrite are heavier than those of typical submarine hydrothermal solutions, which suggests that the second pulse of mineralization was probably derived from a magmatic hydrothermal fluid. In addition, the second pulse of ore-forming fluid has brought some Fe and taken away parts of Zn, which results the lighter δ^{66}Zn values of sphalerite and heavier δ^{56}Fe values of pyrite from the second pulse of mineralization. Overall, the Zhaxikang deposit records two pulses of mineralization, and the overprint by the second pulse of mineralization causes the lighter δ^{66}Zn values and heavier δ^{56}Fe values of modified samples.

1. Introduction

Constraining the source of metal is a fundamental issue in understanding ore deposit formation. Traditional light stable isotopes, such as C, H, O, S, and N isotopes, have been widely used to trace the fluids and sources of metal in ore deposits (Taylor, 1974; Yeh et al., 1999; Mao et al., 2003; Chen et al., 2005; Huang et al., 2015). However, these elements do not represent the main commodities within these deposits and as such can only provide indirect and putative indicators of metal sources. Transition metal stable isotopes (e.g., Fe, Zn and Cu) could provide more direct and accurate information on the sources of metal within ore deposits, given the increased precision of isotopic analyses of these elements resulting from improved Multicollector–Inductively Coupled

* Corresponding authors at: State Key Laboratory of Geological Processes and Mineral Resources, School of Earth Sciences and Mineral Resources, China University of Geosciences, Beijing 100083, China (Y. Zheng).
E-mail addresses: sunxiang8003@sina.com (X. Sun), zhyouye@163.com (Y. Zheng).

http://dx.doi.org/10.1016/j.oregeorev.2016.12.030
0169-1368/

Plasma Mass Spectrometer (MC–ICP–MS) technology (Maréchal et al., 1999; Belshaw et al., 2000). Thus, these non-traditional stable isotopes can be used as potential tracers of processes in metallogenic systems (Wang and Zhu, 2010, 2012; Liu et al., 2014b, 2014c; Li et al., 2015).

Transition metal isotopic analyses (e.g., Fe and Zn) have been widely applied to ore deposits studies (Graham et al., 2004; Markl et al., 2006; Zhu et al., 2008; Kelley et al., 2009; Wang and Zhu, 2010, 2012; Wang et al., 2011, 2012a; Yan et al., 2010; Sun et al., 2012, 2013; Cheng et al., 2013; Hou et al., 2014; Liu et al., 2014a). For example, Markl et al. (2006) determined the Fe isotopic compositions of the Schwarzwald hydrothermal vein deposit in southwest Germany, but suggested that Fe isotopes are inappropriate to identify the sources of metal in ore deposits for two reasons: (1) the Fe isotopic fractionation occurs during geological processes (Johnson et al., 2002; Icopini et al., 2004; Butler et al., 2005; Liu et al., 2014a), and (2) the fractionation of Fe isotopes during these processes remains poorly constrained. However, Wang et al. (2011) used the gradually increasing δ^{56}Fe values from early to late stages and from endoskarn to exoskarn within the Xinqiao skarn Cu–S–Fe–Au deposit to identify the formation of this deposit, suggesting that the iron in the skarn was predominantly derived from igneous rocks rather than sedimentary rocks. Additionally, Sun et al. (2013) used Fe isotopic data of the Bayan Obo Fe-rare earth element (REE) deposit, which has a narrow range in δ^{56}Fe values that cluster at 0‰, to constrain the magmatic origin rather than sedimentary origin or hydrothermal processes. Zhu et al. (2016) also identified Fe isotope fractionation between ore minerals and diorites during skarn-type alteration within the Han–Xing skarn Fe deposit and suggested that the metal was derived from a magmatic hydrothermal system rather than recycled pre-existing mineralization or altered associated igneous rocks. It is concluded that, the hydrothermal deposits have moderate Fe isotopic variation range and relative light δ^{56}Fe values with distinct changes across different stages of mineralization (Wang et al., 2011; Wang and Zhu, 2012). In comparison, the magmatic deposit displays a narrow range in δ^{56}Fe values that cluster at 0‰ (Sun et al., 2013), whereas sedimentary origin BIF deposits show the largest range in δ^{56}Fe values from −2.05‰ to 3.15‰ (Wang and Zhu, 2012).

The gradually increasing trend of δ^{66}Zn values (0‰ and 0.6‰) from early to late stages and from south to north within the Red Dog ore district in Alaska record the temporal and spatial evolution of the mineralizing fluids (Kelley et al., 2009). Mason et al. (2005) and Wilkinson et al. (2005) identified a trend of increasing δ^{66}Zn values from the core to the edge of the Alexandrinka volcanic hosted massive sulphide (VHMS) deposit in Russia and from the early to late stages of Midlands volcanogenic massive sulphide (VMS) deposit in Ireland, respectively. This trend, together with the results of previous research (Archer et al., 2004), indicates that the δ^{66}Zn values of minerals precipitating from the same hydrothermal fluids become heavier over time. In addition, Zhou et al. (2014) compared the δ^{66}Zn values of the Pb–Zn deposits in the Sichuan–Yunnan–Guizhou Pb–Zn metallogenic province with those of other types of Pb–Zn deposits elsewhere, then finally identified unique carbonate-hosted genesis of these deposits. All of the research indicate the potential of Fe and Zn isotopic data to provide insights into the evolution of mineralizing fluids and to constrain the genesis of ore deposit.

The Zhaxikang Sb–Pb–Zn–Ag deposit is the only large deposit identified to date within the North Himalayan Metallogenic Belt (NHMB) of southern Tibet. Although the geology, petrography, geochronology, and geochemistry of this deposit have been extensively studied (Zheng et al., 2012, 2014; Zhu et al., 2012; Liang et al., 2013, 2014; Li et al., 2014), controversies remain due to the complicated mineralogy and the presence of multiple stages of mineralization. The current models for the genesis of the Zhaxikang deposit involved a hot spring (Meng et al., 2008; Zhang et al., 2010) and a magmatic hydrothermal fluid (Wang et al., 2012b). Two pulses of mineralization at the Zhaxikang deposit were recently proposed (Zheng et al., 2012, 2014; Liang et al., 2013, 2014), but are still debated. Zheng et al. (2012, 2014) suggested that the Mn–Fe carbonates in the deposit formed during the first pulse of mineralization, whereas Liang et al. (2014) suggested that these carbonates formed during the second pulse of mineralization, with the first pulse of mineralization dominated by the formation of sphalerite, galena, and only minor amounts of Mn–Fe carbonates. Here, we present new Fe isotopic data for pyrite and Mn–Fe carbonate, and Zn isotopic data for sphalerite, Mn–Fe carbonate, and slate from the Zhaxikang deposit to provide new evidence for the two pulses of mineralization and the sources of metal.

2. Geological setting

2.1. Regional geology

The Himalayan terrane is divided into four tectonic belts (from north to south): the North Himalayan Tethys sedimentary fold belt (TH), the High Himalayan crystalline rock belt (HH), the Low Himalayan fold belt (LH), and the Sub-Himalayan tectonic belt (SH; Fig. 1A; Harrison et al., 1992; Jeffrey et al., 2000; Murphy et al., 2002; Pan et al., 2004, 2006). These belts are separated by three nearly EW-trending faults named the South Tibet Detachment System (STDS), the Main Central Thrust (MCT), and the Main Boundary Thrust (MBT; Fig. 1A; LeFort, 1975; Yin and Harrison, 2000; Spratt et al., 2005). The North Himalayan Tectonic Belt, located to the south of the Indus-Yarlung Zangbo Suture Zone and to the north of the High Himalayan crystalline rock series, is primarily dominated by a set of Palaeozoic marine sedimentary sequences that formed in a passive continental margin environment within northern India (Yu and Wang, 1990).

The Tethys Himalaya sedimentary sequence records Late Precambrian to Devonian pre-rift, Carboniferous to Early Jurassic syn-rift, and Middle Jurassic to Cretaceous passive continental margin sediments (Fig. 1B; Liu and Einsele, 1994; LeFort et al., 1996; Garzanti, 1999). These sediments crop out in an EW and NWW trending area of the north Himalaya and include the Precambrian Laguigangri Group and a series of Upper Triassic, Jurassic, Lower Cretaceous, and Quaternary sediments. The Laguigangri Group contains schist, gneiss, and migmatite units that crop out in the core of the Yelaxiangbo dome (Fig. 1B). A set of Late Triassic-Early Cretaceous flysch formations, deposited in neritic-bathyal environments, also crops out across the study region. This formation is dominated by turbidite deposits and contains weak-metamorphic slate that is intercalated with metamorphosed fine-grained sandstone, argillaceous limestone, micrite, and siliceous rock that is intercalated with volcanic rocks. This formation also hosts the majority of the Au–Sb–Pb–Zn–Ag deposits in this region (Zheng et al., 2012).

Two sets of faults that trend nearly EW and NS are present in the study region and record multiple stages of movement. The EW-trending faults, including the Lazi–Qiongduojiang, Rongbu–Gudui, and Luozha faults as well as the STDS and numerous metamorphic core complexes, cover a larger area than the younger NS-trending faults. These EW-trending faults are also associated with a series of rifts that formed from 25 Ma to present (Molnar and Tapponnier, 1978; Armijo et al., 1986; England and Houseman, 1989; Harrison et al., 1992; Pan and Kidd, 1992; Yin, 2000). These rifts include the Sangri–Cuona, Yadong–Gulu, Shenzha–Xietongmen, and Dangreyongcuo–Gucuo rift zones from east to west (Li et al., 2005; Liang et al., 2013). The NS-trending faults formed dur-

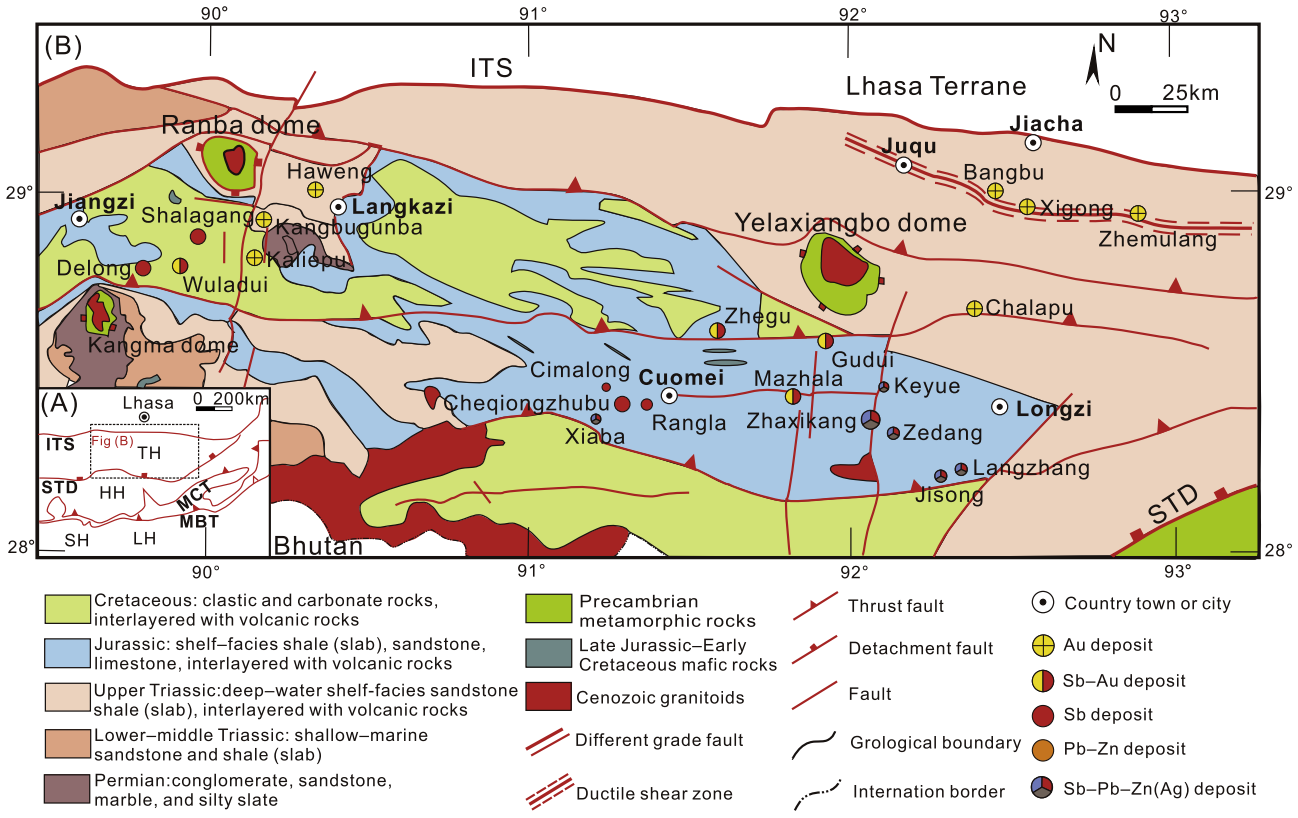

Fig. 1. (A) Tectonic framework of the Himalayan Terrane (modified from Yin, 2000). (B) Regional geological map of the North Himalayan Metallogenic Belt (modified from Zhu et al., 2011; Zheng et al., 2014).

ing the same period as the rifts (18 to 4 Ma; Yin et al., 1999; Blisniuk et al., 2001; Williams et al., 2001) as a result of east–west extension of the Qinghai–Tibet Plateau.

Magmatism in the North Himalaya generated multiple suites of mafic-intermediate igneous rocks between the Late Triassic and the Early Cretaceous, including basaltic volcanic interlayers, dyke swarms, and sub-volcanic dykes. Extensive igneous activity around 132 Ma also formed the Comei–Bunbury large igneous province that crops out in this region (Zhu et al., 2009). The study region also contains widespread Cenozoic igneous rocks that are dominated by monzogranite, leucogranite, diorite, porphyritic diorite, and aplite units (Searle, 1999; Visonà and Lombardo, 2002; Nie et al., 2005; Zhang and Gao, 2005; Zeng et al., 2009, 2012; Zhang et al., 2011). The mineralization in the NHMB is dominated by Au, Sb, Au–Sb, and Sb–Pb–Zn–Ag deposits, including the Zhaxikang Sb–Pb–Zn–Ag, the Mazhala Au–Sb, the Chalapu Au, the Bangbu Au, the Shalagang Sb, and the Cheqiongzhuobu Sb deposits (Zheng et al., 2014).

2.2. Ore deposit geology

The Zhaxikang deposit is located ~27 km west from Ridang Town within the south-eastern Yangzuoyong-Nariyong composite syncline in the North Himalayan tectonic belt (Zhang et al., 2010; Zheng et al., 2012). This deposit has a reserve of 1.268 Mt of Zn and Pb at an average grade of 3.66% Zn and 2.45% Pb. The deposit also contains 0.138 Mt of Sb at an average grade of 1.08% Sb, 1800 t of Ag at a grade of 99.55 g/t Ag, 3.9 t of associated Au, 361 t of associated Ga, and 20 Mt of Mn–Fe carbonate ore at an average grade of 42% Fe + Mn (Zheng et al., 2016). The majority of mineralization in the Zhaxikang deposit is hosted by weak-metamorphic marine clastic sediments of the Lower Jurassic Ridang Formation, which dips shallowly to the north and strikes east–west. The orefield also contains fine-grained metamorphosed quartzose sandstone, silty slate, and calcarenite units of the Upper Jurassic Weimei Formation and some Quaternary sediments (Zheng et al., 2012).

The Zhaxikang deposit is controlled by a series of nearly NS-striking faults that coexist with a set of NE-striking faults and folds. Geological mapping in this area has identified 16 faults, the majority of which are steeply dipping normal faults associated with tensional stress and wrench faults associated with torsional stress. The F2, F4, F5, F6, and F7 faults are associated with mineralization, with faults F1 and F10 hosting mineralization, fault F3 associated with late-stage mineralization, faults F8 and F9 being wrench faults that are free of mineralization, and F12 being a non-mineralized regional fault. Nine Pb–Zn orebodies are associated with the nine mineralized faults in this orefield (Zhang et al., 2010), where orebodies I–VI are hosted by crush zones in nearly NS-striking faults and orebodies VII–IX are hosted by crush zones in nearly NE-striking faults. The majority of the mineralization in the orefield is hosted by orebodies IV and V (Fig. 2). In particular, orebody V, which is controlled by the F7 fault, is >1400 m long, 1–30 m wide, and hosts more than 80% of the reserves within the deposit, making it the largest and richest orebody within the orefield.

The Zhaxikang deposit records magmatism that formed diabase, porphyritic rhyolite, basalt, and leucogranite units as well as some granite porphyry dykes that intruded into the porphyritic rhyolite. The diabase is present as dykes that emplaced into the Jurassic Ridang Formation. Diabase that formed at ~133 Ma (Zheng et al., 2012) also has been found on outcrops, in drillholes and in footrill in the central part of the orefield. The rhyolite porphyry crops out in the southern part of the orefield and has been dated by zircon U–Pb methods to 135 Ma (Lin et al., 2014), almost identical to the age of a rhyolite within the Ridang Formation in the Mazhala ore

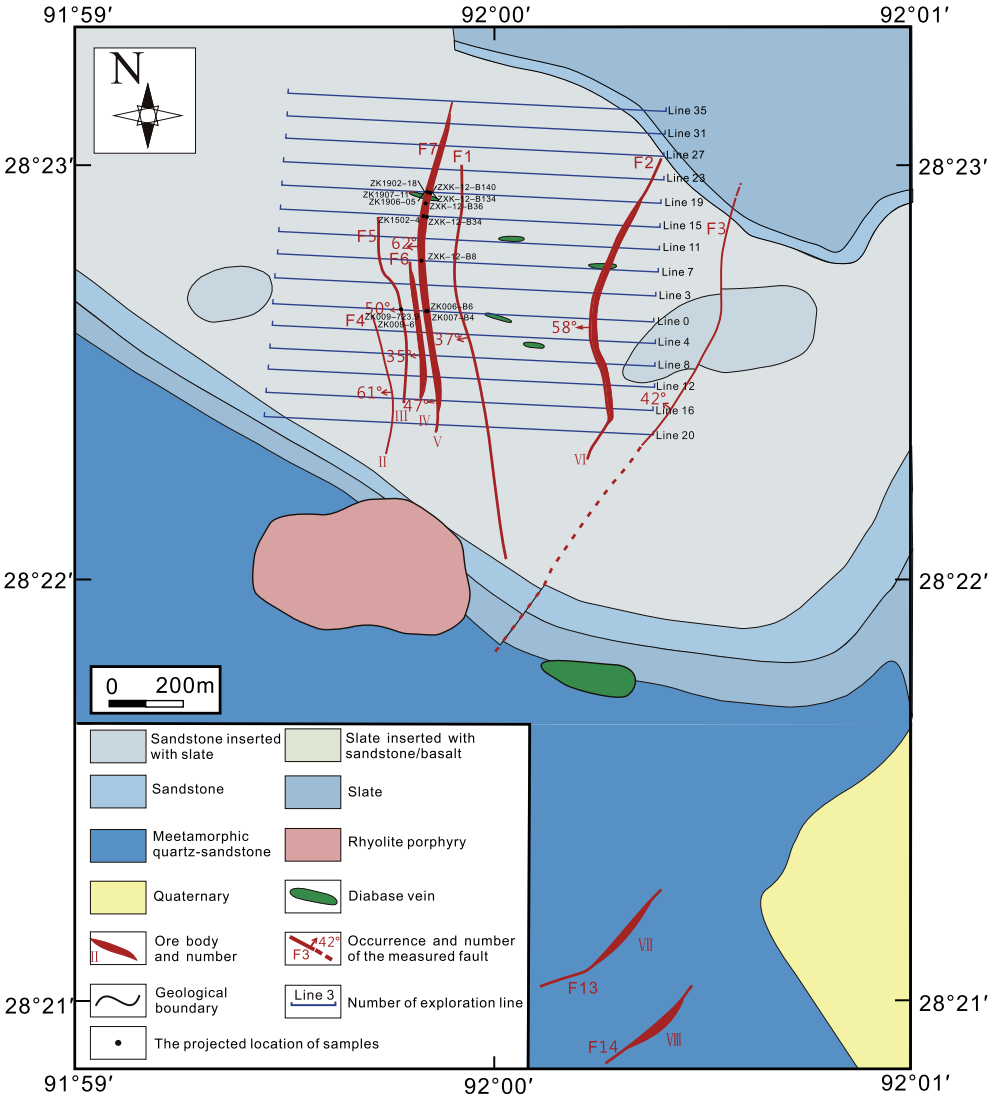

Fig. 2. Geological map of the Zhaxikang Sb–Pb–Zn–Ag polymetallic deposit (modified from Zheng et al., 2012).

deposit. Leucogranite also occurs in the southern part of the orefield.

The mineralization in the Zhaxikang orefield is associated with various types of alteration, including (1) silicification associated with antimony mineralization that is generally located in fault zones in the form of quartz veins, radiating quartz, and quartz druse; (2) carbonate alteration that formed Mn–Fe carbonate veins associated with Pb–Zn mineralization as well as post-mineralization calcite; (3) chlorite alteration that is generally confined to massive and stellated aggregates of chlorite within diabase; (4) weak sericite alteration associated with chlorite alteration and barren quartz; and (5) clay alteration developed along the edges of fracture-related crush zones. The deposit is zoned from a lowermost Zn (Pb + Ag) zone through a central Zn + Pb + Ag-(Sb) zone to an uppermost Pb + Zn + Sb + Ag zone, although no horizontal zoning is present (Zheng et al., 2012, 2016).

3. Ore characteristics and sample selection

The formation of the Zhaxikang deposit can be divided into six stages according to cross-cutting relationships and the paragenesis of minerals (Fig. 3). These stages are assigned to two clear pulses as follows: the first pulse consisting of stages 1 and 2 that is primarily dominated by Mn–Fe carbonates and sulphides, and the second pulse including stages 3–6 that is dominated by quartz, calcite, sulfosalt minerals, and sulphides. A lack of sphalerite and pyrite in stages 4–6 meant that the samples used for Fe–Zn isotope analyses were exclusively obtained from stages 1–3. The ore characteristics and the samples selected for Fe–Zn isotope analyses are described below, and detailed descriptions of the samples that were analyzed in this study are given in Table 1.

Stage 1 is characterized by a Mn–Fe carbonate (molecular formula is $(Mn_{0.5}Fe_{0.5})CO_3$ according to unpublished electron probe data (EPMA), hereafter referred to as 'Mn–Fe carbonate' for simplicity) + sphalerite + pyrite + arsenopyrite assemblage that represents the initial stage of formation of the Zhaxikang deposit. The sphalerite, pyrite, and arsenopyrite that formed during this stage of mineralization are generally fine-grained, with lamellar sphalerite, pyrite, and arsenopyrite hosted by fine-grained Mn–Fe carbonate (Fig. 4A and E), some of which have fine-grained layered and colloform textures (Fig. 4B). A few sulphides are present as stellated aggregates within the Mn–Fe carbonates that formed during this stage (Fig. 4D). Later quartz-boulangerite veins cut both the laminae and the Mn–Fe carbonates (Fig. 4A), and the formation of stage 2 coarse-grained sphalerite has also affected this earlier mineralization (Figs 4A and 5A1).

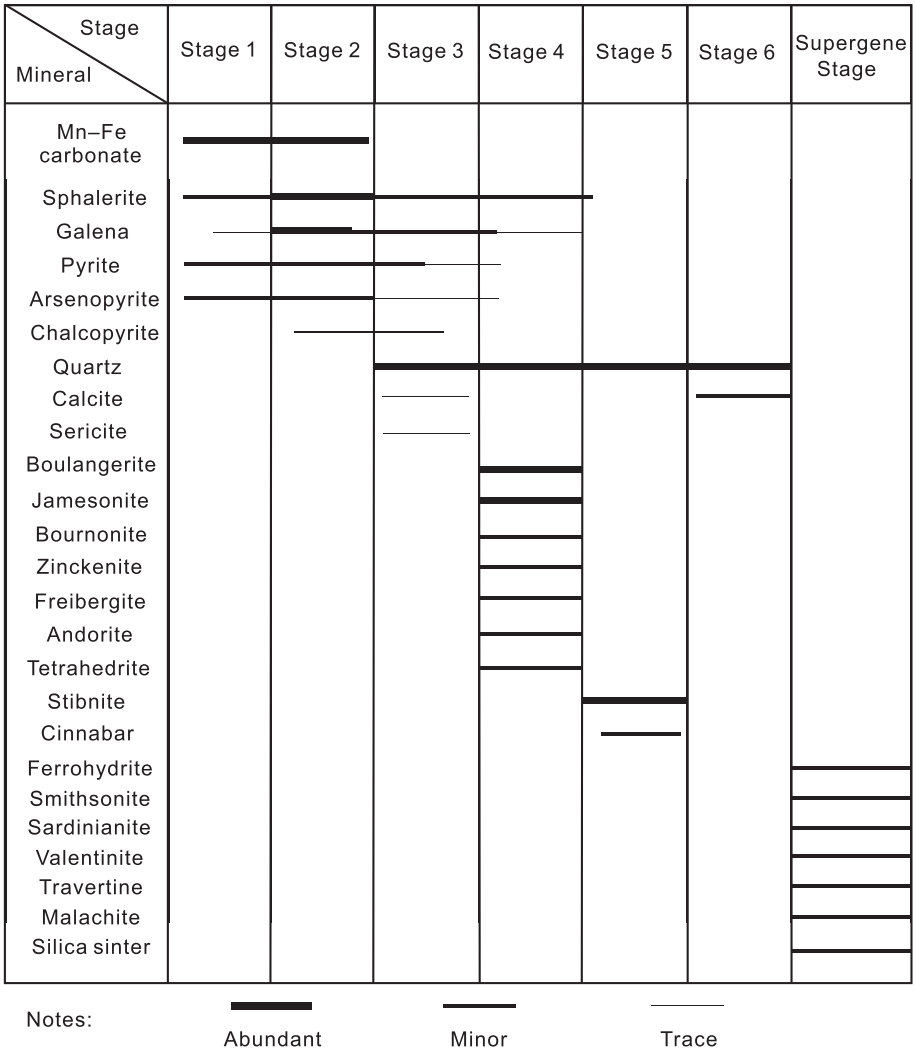

Fig. 3. Mineral paragenesis within the Zhaxikang deposit.

Stage 2 is characterized by the development of a Mn–Fe carbonate + galena + sphalerite + pyrite ± arsenopyrite assemblage that includes coarse-grained sphalerite, galena, and pyrite hosted by Mn–Fe carbonate and slate (Fig. 4C). The minerals that formed during this stage are coarser-grained than those of stage 1 and are hosted by massive, banded, stockwork, brecciated, concentric annular, globular, and disseminated ores (Figs. 4D, F–I and 5B). The Mn–Fe carbonate that formed during this stage is coarse-grained (Fig. 4F–I) and variably recrystallized (Figs 4D and 5A–C). Some of these Mn–Fe carbonates also contain druse filled with idiomorphic columnar quartz, needle-like boulangerite, or valentinite that formed by the oxidation of boulangerite (Fig. 5C4). These characteristics of Mn–Fe carbonate are probably related to the modification of the second pulse of mineralization by later hydrothermal fluids. Early sphalerite and pyrite are also replaced by later galena (Fig. 4S and T). A recrystallized pyrite vein cross-cuts early Mn–Fe carbonate and later sphalerite replaces early pyrite to form a skeletal texture (Fig. 4U). The majority of the Pb–Zn mineralization in the deposit formed during this stage.

Stage 3 is characterized by the formation of a quartz ± calcite + pyrite + sphalerite + galena ± chalcopyrite assemblage without Mn–Fe carbonate and is associated with a gangue dominated by quartz with trace amounts of calcite. The stage 3 sphalerite, galena and minor amounts of pyrite formed by the modification of early-formed sulphides, with euhedral galena and pyrite aggregates also present. Minor amounts of chalcopyrite grains are dotted among the grains of sphalerite, galena and pyrite that formed during this stage. This stage also generated massive, veined, and brecciated black sphalerite (Fig. 4J–M), and the massive galena, pyrite, sphalerite ores of this stage are cross-cut by later quartz–boulangerite or quartz–calcite veins (Fig. 4H, J, and M). The early formed fine-grained pyrite attaches to the crystal or growth planes of coarse-grained pyrite from this stage (Fig. 4Q), providing more evidence of recrystallization that was possibly associated with the overprinting effect of later hydrothermal fluids.

Stage 4 is characterized by a quartz + antimony-lead-silver sulfosalt minerals assemblage that hosts the majority of the Sb and Ag ore within the deposit, yielding ores that have relatively high average Ag grades. The sulfosalt minerals of this stage include boulangerite and jamesonite, with minor bournonite, tetrahedrite, and andorite. Quartz–boulangerite veins and needle-like boulangerite in quartz druse are also present of this stage (Fig. 4A, H, I–J, and N). The boulangerite replaces and cross-cuts minerals formed in earlier stages (Fig. 4R, V, and X). This stage of mineralization also generated minor amounts of sulphides.

Stage 5 is characterized by a quartz + stibnite + cinnabar assemblage that hosts part of the Sb mineralization in the deposit. This stage produces elongate and radial quartz-hosted stibnite (Fig. 4P) that cross-cuts the earlier-formed stage 4 boulangerite (Fig. 4V).

Table 1
Detailed description of the samples used for isotopic analysis during this study.

Sample number	Mineral	δ^{56}Fe	δ^{66}Zn	Sample description	Altitude
ZXK12-PD9-B2	Mcar 1	−0.75	0.32	Stage 1 lamellar sphalerite–pyrite–arsenopyrite and stage 2 massive sphalerite–pyrite hosted within fine-grained Mn–Fe carbonate.	Unknown
	Py 1	−0.31			
	Py 2	−0.30			
	Sp 1		0.29		
	Sp 2		0.09		
D52-3	Mcar 1	−0.62		Stage 1 lamellar sphalerite–pyrite–arsenopyrite and stage 2 massive and banded sphalerite–pyrite hosted by fine-grained Mn–Fe carbonate. The mineral assemblages is in turn cross-cut by stage 4 quartz–boulangerite veins.	Unknown
	Py 1	−0.09			
	Py 2	0.13			
	Sp 1		0.16		
14-6	Mcar 1	−0.68		Stage 1 lamellar sphalerite–pyrite–arsenopyrite and stage 2 massive sphalerite hosted by fine-grained Mn–Fe carbonate.	Unknown
	Py 1	−0.27			
	Sp 1		0.35		
14-9	Mcar 1	−0.65	0.17	Stage 1 lamellar sphalerite–pyrite–arsenopyrite and stage 2 massive sphalerite hosted by fine-grained Mn–Fe carbonate. The sample also contains a Mn–Fe carbonate druse with idiomorphic columnar quartz and valentinite formed by the oxidation of boulangerite.	Unknown
	Py 1	−0.33			
	Sp 1		0.32		
ZXK-12-B8	Mcar 2	−0.63		Massive Stage 2 coarse–grained sphalerite–pyrite hosted by stage 2 Mn–Fe carbonate and slate. The sample also contains minor amounts of stage 6 quartz and calcite.	4575m
ZXK-12-B156	Mcar 2	−0.59	0.24	Massive ore containing stage 2 slightly recrystallized Mn−Fe carbonate, stage 2 coarse-grained sphalerite–pyrite and minor amounts of quartz grains.	Unknown
	Py 2	0.19			
	Sp 2		0.20		
ZXK-12-B134	Mcar 2	−0.80		Massive ore containing slightly recrystallized stage 2 Mn–Fe carbonate, stage 2 coarse–grained sphalerite–galena–pyrite and minor amounts of quartz grains.	4575m
	Py 2	0.02			
ZXK-12-B34	Mcar 2	−0.63	0.26	Stage 2 banded coarse-grained sphalerite–pyrite hosted by slightly recrystallized stage 2 Mn–Fe carbonate and slate.	4575m
	Sp 2		0.23		
ZK006-B6	Mcar 2	−0.55		Stage 3 brecciated coarse-grained sphalerite hosted by stage 3 quartz. The sample also contains globular stage 1 Mn–Fe carbonate breccia containing stage 1 sphalerite–pyrite–arsenopyrite cemented by stage 2 Mn–Fe carbonate.	4255m
	Sp 3		0.16		
ZK1902-18	Mcar 2	−0.58		Massive coarse-grained sphalerite hosted by Mn–Fe carbonates and mineralized slate. The sample also contains numerous stage 2 Mn–Fe carbonate–pyrite–sphalerite–galena stringers.	4509m
ZK1906-05	Mcar 2	−0.73		Stage 2 massive coarse-grained sphalerite–pyrite hosted by stage 2 Mn–Fe carbonate and slate, with the latter cross-cut by a stage 4 pyrite–quartz–boulangerite vein.	4187m
ZK1907-11	Mcar 2	−0.61		Stage 2 pyrite stellated aggregates hosted by slate associated with and partially replaced by stage 2 Mn–Fe carbonate. The carbonates are cross-cut by a stage 4 quartz–boulangerite vein.	4094m
ZXK-12-B140	Py 2	0.08		Stage 1 lamellar sphalerite–pyrite–arsenopyrite and stage 2 massive coarse-grained sphalerite–pyrite within Mn–Fe carbonates.	4575m
ZXK-12-B154	Py 3	0.23		Massive ore containing recrystallized stage 2 Mn–Fe carbonates, stage 3 coarse-grained sphalerite–galena–pyrite, and significant amounts of quartz.	Unknown
ZK1502-4	Py 3	0.43		Massive ore containing stage 3 coarse-grained galena and pyrite that is cross–cut by stage 6 quartz veins.	4422m
XC-2	Py 3	0.41		Stage 3 disseminated pyrite within a large blocky mass of stage 3 sphalerite. The sample also contains Mn–Fe carbonate–pyrite–sphalerite cross-cut by a stage 4 quartz–boulangerite vein.	Unknown
XC-3	Py 3	0.36		Stage 3 banded pyrite hosted by a large blocky mass of stage 3 sphalerite. This is in turn cross-cut by a stage 4 quartz–boulangerite vein and a boulangerite-bearing quartz druse. The sample also contains minor amounts of early Mn–Fe carbonate.	Unknown
XC-6	Py 3	0.16		Stage 3 sphalerite cross-cut by stockwork-type quartz veins and containing minor amounts of stage 3 pyrite present as stellated aggregates. The sample also contains minor amounts of Mn–Fe carbonate.	Unknown
ZXK-12-B36	Sp 3		−0.03	Stage 3 massive coarse-grained sphalerite and stockwork-type pyrite veins within recrystallized stage 2 Mn–Fe carbonate. The sample also contains quartz druses and quartz–pyrite veins.	4575m
ZXK-BDG-3	Sp 2		0.16	Disseminated stage 2 globular and brecciated coarse-grained sphalerite within stage 2 Mn–Fe carbonate with the typical Dalmatian structure. The sample also contains stage 2 massive coarse-grained pyrite hosted by stage 2 Mn–Fe carbonate and sphalerite as well as pyrite present as stellated aggregates.	Unknown
ZK009-723.9	Sp 3		0.22	Stage 3 quartz-hosted massive coarse-grained sphalerite-pyrite. The sample also contains minor amounts of Mn–Fe carbonate.	4169m
ZK009-6	Sp 3		0.16	Stage 3 quartz-hosted massive coarse-grained sphalerite–pyrite. The sample also contains minor amounts of Mn–Fe carbonate.	4161m
HY	Sp 3		0.09	Stage 3 quartz-hosted massive coarse-grained sphalerite–pyrite.	Unknown
ZXK-12-B84	Sp 3		0.09	Stage 3 coarse–grained sphalerite and pyrite cross–cut by stage 4 quartz–stibnite–galena–sulfosalt veins.	4570m
ZK007-B4	Sp 3		0.21	Stage 3 brecciated and massive sphalerite–galena hosted by stage 3 calcite. The sample also contains stage 3 disseminated pyrite hosted by sphalerite.	Unknown
ZXK-11-17	Slate		0.08	Stage 3 slate-hosted massive sphalerite. The sample also contains a late-stage mass of stibnite–boulangerite that is hosted by the sphalerite.	Unknown
ZXK-11-31	Slate		0.05	Slate cross-cut by a quartz vein, both of which host stellated aggregates of stage 3 sphalerite–pyrite.	Unknown
ZXK-12-B17	Slate		0.38	Slate cross-cut by Mn–Fe carbonate veins, both of which host stellated aggregates of stage 2 sphalerite–pyrite.	Unknown
PD6-50	Slate		0.12	Slate cross-cut by quartz veins, both of which host stellated aggregates of stage 3 sphalerite–pyrite.	Unknown

Abbreviations are as follows: Mcar 1: stage 1 Mn–Fe carbonate, Mcar 2: stage 2 Mn-Fe carbonate, Py 1: stage 1 pyrite, Py 2: stage 2 pyrite, Py 3: stage 3 pyrite, Sp 1: stage 1 sphalerite, Sp 2: stage 2 sphalerite, Sp 3: stage 3 sphalerite.

Stage 6 is characterized by a quartz ± calcite assemblage that is free of sulphides and cross-cuts earlier formed ores (Fig. 4M, V–W).

Four samples from stage 1 were analyzed, with Fe–Zn isotopic analyses on Mn–Fe carbonate, lamellar pyrite and sphalerite (Table 1). The laminae within sample D52–3 is cross-cut by a

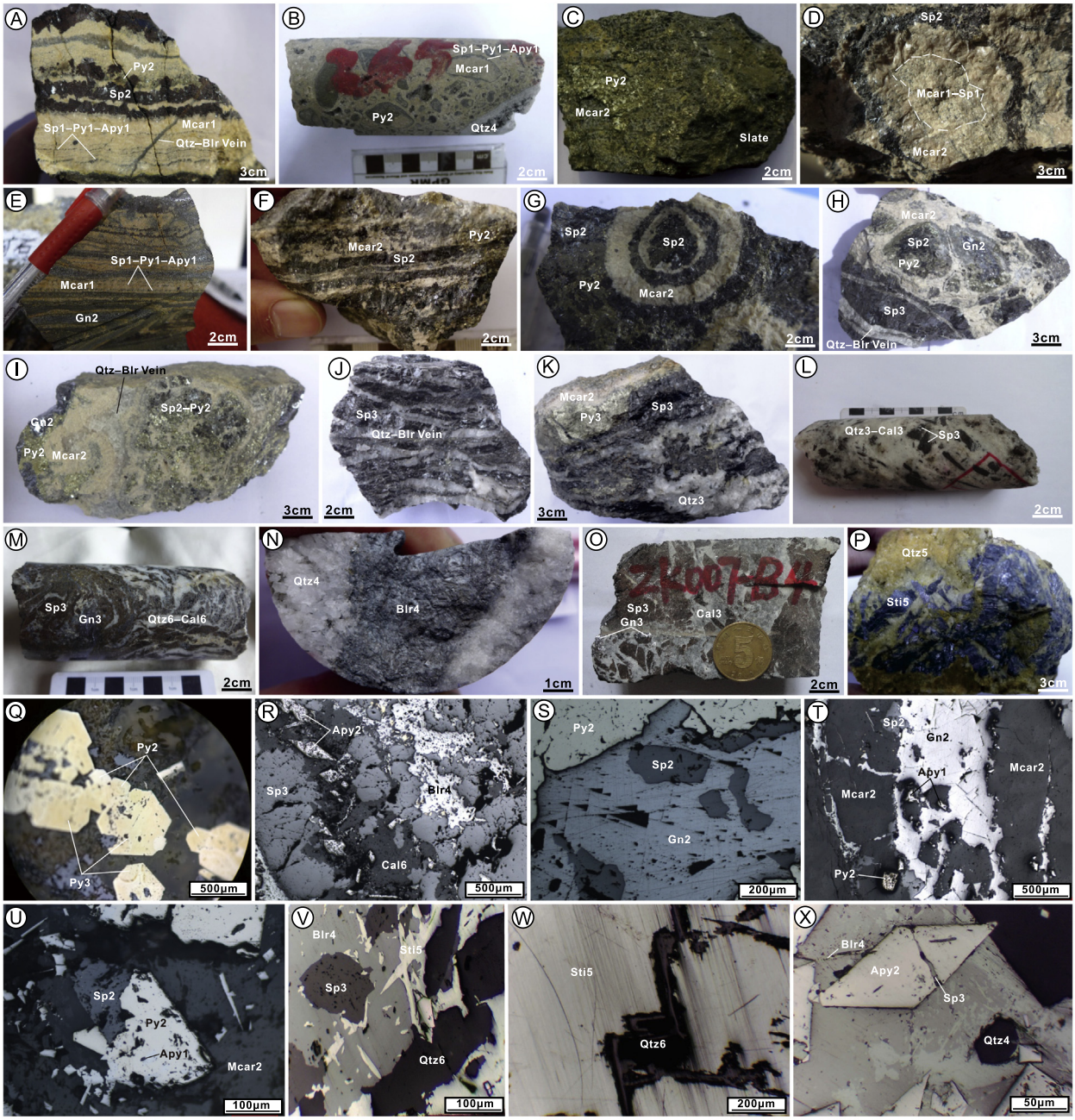

Fig. 4. Hand specimen photographs and photomicrographs of representative samples from the Zhaxikang deposit. (A) Stage 1 lamellar sphalerite–pyrite–arsenopyrite and stage 2 massive and banded sphalerite–pyrite hosted by fine-grained Mn–Fe carbonate. The mineral assemblages is in turn cross-cut by stage 4 quartz–boulangerite veins. (B) Globular stage 1 Mn–Fe carbonate breccia containing stage 1 sphalerite–pyrite–arsenopyrite cemented by stage 2 Mn–Fe carbonate. (C) Stage 2 massive coarse-grained pyrite hosted by slate and stage 2 Mn–Fe carbonate. (D) Coarse-grained stage 2 Mn–Fe carbonate–sphalerite formed by the recrystallization of fine-grained stage 1 Mn–Fe carbonate–sphalerite. (E) Stage 2 lamellar and banded Mn–Fe carbonate–sphalerite–galena ore with visible synsedimentary features including rhythmic sedimentation in the upper part of the sample and angular folding in the lower part. (F) Stage 2 coarse-grained sphalerite–pyrite hosted by stage 2 Mn–Fe carbonate with banded textures. (G) Stage 2 coarse-grained sphalerite–pyrite hosted by stage 2 Mn–Fe carbonate with massive and concentric annular textures. (H) Stage 2 coarse-grained sphalerite–pyrite hosted by stage 2 Mn–Fe carbonate with massive and globular textures. The sample also contains stage 3 sphalerite cross-cut by stage 4 quartz–boulangerite veins. (I) Stage 2 massive and disseminated sphalerite–galena–pyrite within stage 2 Mn–Fe carbonate that is cross-cut by a later stage 4 quartz–boulangerite vein. (J) Stage 3 sphalerite cross-cut by stage 4 quartz–boulangerite veins. (K) Stage 3 banded pyrite hosted by a large blocky mass of stage 3 sphalerite that is in turn cross-cut by a stage 4 quartz–boulangerite vein. The sample also contains some early Mn–Fe carbonates and quartz druse that contain boulangerite. (L) Stage 3 brecciated sphalerite within stage 3 quartz–calcite. (M) Stage 3 sphalerite–galena veins cross-cut by stage 6 quartz–calcite veins. (N) Stage 4 quartz–boulangerite vein. (O) Stage 3 brecciated and massive sphalerite–galena hosted by stage 3 calcite. (P) Elongate stage 5 stibnite hosted by stage 5 quartz. (Q) Stage 2 fine-grained pyrite attaches to the crystal or growth planes of stage 3 coarse-grained pyrite. (R) Stage 3 sphalerite cross-cut and replaced by stage 4 boulangerite. (S) Stage 2 sphalerite replaced by stage 2 galena to form a relict texture. (T) Stage 2 Mn–Fe carbonate–sphalerite with embayed structures as a result of replacement by stage 2 galena. (U) Stage 2 pyrite containing automorphic stage 1 arsenopyrite replaced by later stage 2 sphalerite to form a skeletal texture. (V) Stage 3 sphalerite replaced by stage 4 boulangerite that is in turn cross-cut by stage 5 stibnite. (W) Stage 5 stibnite cross-cut by stage 6 quartz. (X) Stage 2 arsenopyrite cross-cut by a stage 3 sphalerite vein and stage 3 sphalerite cross-cut by a stage 4 boulangerite vein. Abbreviations are as follows: Mcar 1: stage 1 fine-grained Mn–Fe carbonate; Apy 1: stage 1 lamellar arsenopyrite; Py 1: stage 1 lamellar pyrite; Sp 1: stage 1 lamellar sphalerite; Mcar 2: stage 2 coarse-grained Mn–Fe carbonate; Apy 2: stage 2 arsenopyrite; Py 2: stage 2 pyrite; Sp 2: stage 2 sphalerite; Gn 2: stage 2 coarse-grained galena; Py 3: stage 3 pyrite; Sp 3: stage 3 sphalerite; Gn 3: stage 3 galena; Qtz 3: stage 3 quartz; Cal 3: stage 3 calcite; Blr 4: stage 4 boulangerite; Qtz 4: stage 4 quartz; Sti 5: stage 5 stibnite; Qtz 5: stage 5 quartz; Cal 6: stage 6 calcite; Qtz 6: stage 6 quartz.

Fig. 5. (A) Relationship between increasing alteration of samples and heavier δ^{56}Fe values of pyrite. (B) Relationship between increasing alteration of samples and lighter δ^{66}Zn values of sphalerite. (C) Relationship between increasing alteration of samples and lighter δ^{66}Zn values of Mn–Fe carbonate. (D) Relationship between increasing alteration of samples and lighter δ^{66}Zn values of slate. Abbreviations are as in Fig. 4.

quartz–boulangerite vein (Fig. 4A) and sample 14-9 contains later minerals such as quartz and valentinite (Fig. 5C4). For stage 2, Fe isotopic analysis was performed on eight samples of Mn–Fe carbonate and five samples of pyrite, and Zn isotopic analysis was performed on two samples of Mn–Fe carbonate and four samples of sphalerite (Table 1). Five pyrite and seven sphalerite samples were selected from stage 3 for Fe–Zn isotopic analyses (Table 1). These samples include brecciated sphalerite and galena hosted by calcite in sample ZK007-B6 (Fig. 4O), and massive and veined sulphides hosted by quartz in sample XC-3 (Fig. 4K). Meanwhile, four slate

samples were selected for Zn isotopic analysis: samples ZXK-11-31 and PD6-50 are cross-cut by later quartz–pyrite veins, sample ZXK-11-17 is overprinted by later-stage mineralization including stage 4 boulangerite and stage 5 stibnite, and sample ZXK-12-B17 is cross-cut by a stage 2 Mn–Fe carbonate–pyrite–sphalerite vein (Fig. 5D).

4. Analytical methods

The Fe–Zn isotopic experiments were both carried out in the State Key Laboratory of Geological Processes and Mineral Resources, China University of Geosciences, Beijing. The chemical treatment of the samples was done in a super-clean laboratory. All experimental vessels are PTFE (Savillex®) that were thoroughly cleaned before each use. Double-distilled HCl and HNO_3, Optima™ ultrapure HF and $HClO_4$, and $\geqslant$18.2 MΩ water were used for sample dissolution and all other procedures.

4.1. Chemical separation of iron and zinc

Slate and Mn–Fe carbonate powders (5–30 mg) were dissolved in Teflon vessels with a mixture of HF–HNO_3–$HClO_4$ at 130 °C. After dissolution the solutions were dried and HF was removed before the Teflon vessels were filled with a mixture of HNO_3–HCl. Pyrite and sphalerite sample powders (1–2 mg) were directly dissolved to completion in a mixture of HNO_3–HCl. Then the completely dissolved slate, Mn–Fe carbonate, pyrite and sphalerite samples were heated until they decoloured at 90 °C, and were then evaporated to dryness at 130 °C. All the above processes were repeated one time for the slate and Mn–Fe carbonate samples. The resulting evaporated samples were mixed with 0.5 ml of concentrated HCl (for Fe isotopic analysis) or 1 ml of 8 N HCl (for Zn isotopic analysis) in the same Teflon vessels and brought to dryness. Finally, the dissolved samples were prepared in 0.5 ml of 6 N HCl (for iron isotopic analysis) or 1 ml of 8 N HCl + 0.001% H_2O_2 (for zinc isotopic analysis) for chemical ion exchange separation.

A Bio-Rad AG1X-8 200–400 mesh chloride form resin was used to purify Fe in an HCl media. The matrix elements were removed using 8 ml of 6 N HCl. The iron within these samples was then collected using 9 ml of 0.4 N HCl. These purification procedures were repeated to ensure the complete elimination of the matrices. After evaporating to dryness at 80 °C, the final iron eluate was acidified with 100 μl of concentrated HNO_3 to remove chloride ions before drying and then was dissolved in 3% HNO_3 for isotopic analysis. Zinc was purified using an AG-MP-1M resin with matrix elements removed using 10 ml of 8 N HCl + 0.001% H_2O_2. Copper was then removed using 24 ml of 8 N HCl + 0.001% H_2O_2 before iron was removed using 18 ml of 2 N HCl + 0.001% H_2O_2. Zinc was collected after removing 2 ml of 0.5 N HNO_3, yielding 10 ml of Zn-bearing 0.5 N HNO_3. These purification procedures were repeated for slate and Mn–Fe carbonate samples to ensure the complete elimination of the matrices. Chloride ions were then removed by acidifying the final Zn eluate using 3% (m/m) HNO_3 after being evaporated to dryness at 80 °C. The dried samples were finally dissolved in 3% HNO_3 for isotopic analysis. The samples were checked for the elimination of matrix elements prior to Zn isotopic analysis.

4.2. Fe and Zn isotope determinations

Iron and zinc isotopic analyses were conducted on a Thermo-Finnigan Neptune Plus MC-ICP-MS instrument in the Isotope Geochemistry Laboratory, China University of Geosciences, Beijing. The Fe isotopic measurements were performed in high mass resolution mode and Zn isotopic measurements were performed in low-resolution mode. The sample-standard bracketing (SSB) method was used to correct for instrument mass bias.

4.2.1. Fe isotopes

Samples and standard solutions were prepared in 3% HNO_3 (ca. 0.35 mol l^{-1}), yielding Fe concentrations ranging between 3 and 10 μg ml^{-1} for the high mass resolution mode (HR) analysis. The 3% HNO_3 was measured as a blank only at the beginning of a sequence with on-peak zero correction on samples performed for each analysis. The resulting isotopic compositions are an average of four repeated analyses. A GSB Fe ultrapure single elemental standard solution from the China Iron and Steel Research Institute was used as an in-house reference solution for most of the analyses. Isotope compositions are reported in per mil deviation δ^XFe relative to international standard substance IRMM-014 and analytical uncertainties for δ^{56}Fe are within 0.03‰. The formulas used are as follows:

$$\delta^{56}\mathrm{Fe}\ (\%) = [(^{56}\mathrm{Fe}/^{54}\mathrm{Fe})_{\mathrm{sample}}/(^{56}\mathrm{Fe}/^{54}\mathrm{Fe})_{\mathrm{IRMM\text{-}014}} - 1] \times 1000$$

$$\delta^{57}\mathrm{Fe}\ (\%) = [(^{57}\mathrm{Fe}/^{54}\mathrm{Fe})_{\mathrm{sample}}/(^{57}\mathrm{Fe}/^{54}\mathrm{Fe})_{\mathrm{IRMM\text{-}014}} - 1] \times 1000$$

A BHVO-2 basalt standard and a COQ-1 igneous carbonatite standard of the United States Geological Survey (USGS) were used to assess Fe isotope data quality, with analytical δ^{56}Fe values for BHVO-2 (0.12 ± 0.03‰, 2 se) and COQ-1 (−0.03 ± 0.03‰, 2 se) matching the long-term mean values (BHVO-2: 0.12 ± 0.03‰, N = 27; COQ-1: −0.07 ± 0.03‰, N = 6) from analyses at the same laboratory (He et al., 2015). The Fe content of whole course blank used in these analyses was 16 ng. Further details of the procedures are given by He et al. (2015).

4.2.2. Zn isotopes

The samples and standards used for Zn isotopic analyses were prepared in 3% HNO_3, yielding Zn concentrations of ~ 200 ppb. Each measurement was operated over three blocks of 40 cycles in low-resolution mode with the resulting zinc isotopic ratios reported against the JMC3-0749L standard. The accuracy of the δ^{66}Zn measurements is within 0.06‰ and the formulas used are as follows:

$$\delta^{66}\mathrm{Zn}\ (\%) = [(^{66}\mathrm{Zn}/^{64}\mathrm{Zn})_{\mathrm{sample}}/(^{66}\mathrm{Zn}/^{64}\mathrm{Zn})_{\mathrm{JMC\ 3\text{-}0749\ L}} - 1] \times 1000$$

$$\delta^{68}\mathrm{Zn}\ (\%) = [(^{68}\mathrm{Zn}/^{64}\mathrm{Zn})_{\mathrm{sample}}/(^{68}\mathrm{Zn}/^{64}\mathrm{Zn})_{\mathrm{JMC\ 3\text{-}0749\ L}} - 1] \times 1000$$

A BHVO-2 basalt standard and a BCR-2 basalt standard of the USGS were used to control the Zn isotope data quality, yielding the analytical δ^{66}Zn values (BHVO-2: 0.34 ± 0.13‰, 2 se; BCR-2: 0.33 ± 0.17‰, 2 se) that match the long-term mean values (BHVO-2: 0.33 ± 0.06‰, N = 12; BCR-2: 0.28 ± 0.04‰, N = 4) derived from the same laboratory (Lv et al., 2015). The whole course blank used during these analyses contain 7 ng Zn. For details of these procedures, see Lv et al. (2015) and Liu et al. (2016).

5. Results

The Fe and Zn isotopic data are given in Tables 2 and 3, respectively

5.1. Fe isotopes

All of the Fe isotopic data from the Zhaxikang deposit are plotted on a ternary isotope diagram that yield a single mass-fractionation line with a slope of 0.68. The correlation between δ^{56}Fe and δ^{57}Fe values takes the form $\delta^{56}\mathrm{Fe} = (0.6817 + 0.0026) \times \delta^{57}\mathrm{Fe}$, with an R^2 value of 0.999, indicating that these analyses are free of analytical artefacts from unresolved isobaric interfer-

Table 2
Fe isotopic data for samples from the Zhaxikang deposit.

Sample number	Mineral	δ^{56}Fe	2se	2se*	δ^{57}Fe	2se
ZXK12-PD9-B2	Mcar 1	−0.75	0.02	0.02	−1.13	0.04
	Py 1	−0.31	0.03	0.02	−0.49	0.04
	Py 2	−0.30	0.04	0.04	−0.44	0.06
D52-3	Mcar 1	−0.62	0.02	0.03	−0.92	0.04
	Py 1	−0.09	0.03	0.03	−0.08	0.04
	Py 2	0.13	0.03	0.04	0.17	0.07
14-6	Mcar 1	−0.68	0.02	0.02	−0.98	0.04
	Py 1	−0.27	0.02	0.01	−0.42	0.04
14-9	Mcar 1	−0.65	0.02	0.05	−0.93	0.04
	Py 1	−0.33	0.02	0.02	−0.49	0.04
ZXK-12-B8	Mcar 2	−0.63	0.03	0.02	−0.93	0.04
ZXK-12-B156	Mcar 2	−0.59	0.03	0.02	−0.87	0.04
	Py 2	0.19	0.03	0.02	0.29	0.04
ZXK-12-B134	Mcar 2	−0.80	0.03	0.02	−1.17	0.04
	Py 2	0.02	0.03	0.02	0.02	0.04
ZXK-12-B34	Mcar 2	−0.63	0.03	0.01	−0.93	0.04
ZK006-B6	Mcar 2	−0.55	0.03	0.02	−0.78	0.04
ZK1902-18	Mcar 2	−0.58	0.03	0.02	−0.84	0.04
ZK1906-05	Mcar 2	−0.73	0.03	0.04	−1.09	0.04
ZK1907-11	Mcar 2	−0.61	0.03	0.02	−0.91	0.04
ZXK-12-B140	Py 2	0.08	0.03	0.05	0.13	0.06
ZXK-12-B154	Py 3	0.23	0.03	0.02	0.36	0.04
ZK1502-4	Py 3	0.43	0.03	0.01	0.61	0.04
XC-2	Py 3	0.41	0.03	0.02	0.58	0.04
XC-3	Py 3	0.36	0.03	0.02	0.51	0.04
XC-6	Py 3	0.16	0.03	0.01	0.23	0.04

Notes: Abbreviations are as in Table 1.

Table 3
Zn isotopic data for samples from the Zhaxikang deposit.

Sample number	Mineral	δ^{66}Zn	2sd	δ^{68}Zn
14-6	Sp 1	0.35	0.04	0.68
D52-3	Sp 1	0.16	0.02	0.33
14-9	Sp 1	0.32	0.01	0.63
	Mcar 1	0.17	0.05	0.35
ZXK12-PD9-B2	Sp 1	0.29	0.11	0.58
	Sp 2	0.09	0.04	0.18
	Mcar 1	0.32	0.14	0.64
ZXK-12-B34	Sp 2	0.23	0.08	0.47
	Mcar 2	0.26	0.05	0.49
ZXK-12-B156	Sp 2	0.20	0.06	0.41
	Mcar 2	0.24	0.05	0.45
ZXK-BDG-3	Sp 2	0.16	0.02	0.33
ZXK-12-B36	Sp 3	−0.03	0.06	−0.06
ZK009-723.9	Sp 3	0.22	0.01	0.38
ZK007-B4	Sp 3	0.21	0.06	0.38
ZK009-6	Sp 3	0.16	0.02	0.32
ZK006-B6	Sp 3	0.16	0.01	0.31
HY	Sp 3	0.09	0.07	0.18
ZXK-12-B84	Sp 3	0.09	0.02	0.19
ZXK-11-17	Slate	0.08	0.13	0.16
ZXK-11-31	Slate	0.05	0.05	0.11
ZXK-12-B17	Slate	0.38	0.06	0.75
PD6-50	Slate	0.12	0.13	0.23

Notes: Abbreviations are as in Table 1.

ences. The δ^{56}Fe values of the samples from the Zhaxikang deposit range between −0.80‰ and 0.43‰, with an average value of −0.27‰ ± 0.82‰ (2SD, n = 26). The δ^{56}Fe values of the stage 1 Mn–Fe carbonates range from −0.75‰ to −0.62‰ with an average value of −0.67‰ ± 0.11‰ (2SD, n = 4), and of the stage 2 Mn–Fe carbonates range from −0.80‰ to −0.55‰ with an average value of −0.64‰ ± 0.17‰ (2SD, n = 8). These indicate there are no significant differences in the δ^{56}Fe values of the stage 1 and 2 Mn–Fe carbonates. The stage 1 lamellar pyrite that coexists with fine-grained Mn–Fe carbonate, sphalerite, and arsenopyrite yields δ^{56}Fe values of −0.33‰ to −0.09‰ with an average value of −0.25‰ ± 0.22‰ (2SD, n = 4). In comparison, the stage 2 pyrite that coexists with coarse-grained Mn–Fe carbonate, sphalerite, and galena shows δ^{56}Fe values of −0.30‰ to 0.19‰ with an average value of 0.02‰ ± 0.38‰ (2SD, n = 5). The stage 3 pyrite associated with sphalerite, galena, and quartz has δ^{56}Fe values of 0.16‰–0.43‰ with an average value of 0.32‰ ± 0.24‰ (2SD, n = 5). For the stage 3 modified samples, the δ^{56}Fe values of pyrite are closely related to the modification (Fig. 5A). The most significantly modified sample ZK1502-4 has the heaviest pyrite δ^{56}Fe value of 0.43‰, then the intensely modified samples XC-2 and XC-3 show the heavier pyrite δ^{56}Fe values of 0.41‰ and 0.36‰, respectively, and the slightly modified samples ZXK-12-B154 and XC-6 display the relatively lighter pyrite δ^{56}Fe values of 0.23‰ and 0.16‰, respectively (Tables 1 and 2).

5.2. Zn isotopes

All of the Zn isotopic data from the Zhaxikang deposit are plotted on a ternary isotope diagram that yield a single mass-fractionation line with a slope of 0.51. The correlation between δ^{66}Zn and δ^{68}Zn values yields the formula $\delta^{66}Zn = (0.5128 - 0.0009) \times \delta^{68}Zn$ with an R^2 value of 0.995, which indicates these analyses are free of analytical artefacts from unresolved isobaric interferences. The δ^{66}Zn values of sphalerite throughout the Zhaxikang deposit range from −0.03‰ to 0.35‰ with an average value of 0.18‰ ± 0.20‰ (2SD, n = 15). The stage 1 lamellar sphalerite that coexists with fine-grained Mn–Fe carbonate, pyrite, and arsenopyrite has δ^{66}Zn values of 0.16‰–0.35‰ with an average value of 0.28‰ ± 0.17‰ (2SD, n = 4), whereas the stage 2 sphalerite that coexists with coarse-grained Mn–Fe carbonate, pyrite, and galena shows δ^{66}Zn values of 0.09‰–0.23‰ with an average value of 0.17‰ ± 0.12‰ (2SD, n = 4). In comparison, the stage 3 sphalerite associated with pyrite, galena and quartz displays δ^{66}Zn values that range from −0.03‰ to 0.22‰ with an average value of 0.13‰ ± 0.17‰ (2SD, n = 7). For the stage 3 modified samples, the more significantly modified samples yield lighter sphalerite δ^{66}Zn values (Fig. 5B). The most significantly modified sample ZXK-12-B36 displays the lightest sphalerite δ^{66}Zn value of −0.03‰, then the intensely modified samples ZXK-12-B84 and

HY both show the lighter sphalerite $\delta^{66}Zn$ value of 0.09‰, and the slightly modified samples ZK009-723.9, ZK007-B4 and ZK009-6 has the relatively heavier sphalerite $\delta^{66}Zn$ values of 0.22‰, 0.21‰ and 0.16‰, respectively (Table 1 and 3). Additionally, the Mn–Fe carbonates and slate show $\delta^{66}Zn$ values of 0.17‰–0.32‰ (average value of 0.25‰ ± 0.12‰; 2SD, n = 4) and 0.05‰–0.38‰ (average value of 0.16‰ ± 0.30‰; 2SD, n = 4), respectively.

6. Discussion

6.1. Isotope fractionation between ore minerals

Isotopic fractionation between minerals is a critical issue in isotope research. Observations of hand specimens (Fig. 4A–E) and thin sections (Fig. 4L and O) of Mn–Fe carbonate and sulphides from stages 1 and 2 of the Zhaxikang deposit indicate they closely coexist. In addition, the ores and Mn–Fe carbonates from stages 1 and 2 have similar REE and trace element compositions (Zhang, 2013). Meanwhile, the pyrite, sphalerite, and Mn–Fe carbonate that formed during these stages show similar He–Ar isotope values that overlap with those of crustal fluids (Zhang, 2013). All of the evidence suggest that these early formed Mn–Fe carbonates and sulphides formed contemporaneously from the same source. Here, we investigate the fractionation of Fe and Zn isotopes between Mn–Fe carbonate and pyrite, and Mn–Fe carbonate and sphalerite mineral pairs.

6.1.1. Fe isotope fractionation between Mn–Fe carbonate and pyrite

A $\delta^{56}Fe$–$\delta^{56}Fe$ diagram showing the compositions of various minerals is typically used to determine whether mineral pairs have attained Fe isotopic equilibrium. Here, we use six Mn–Fe carbonate and pyrite mineral pairs (four from stage 1 and two from stage 2) to check whether these minerals were in Fe isotopic equilibrium. The four data points for the stage 1 mineral pairs are highly concentrated, whereas the other two mineral pairs do not provide enough information to draw any conclusions. The $\Delta^{56}Fe_{pyrite-Mn-Fe\ carbonate}$ values for stage 1 samples are 0.44‰ (ZXK12-PD9-B2), 0.53‰ (D52-3), 0.41‰ (14-6) and 0.32‰ (14-9), respectively. Meanwhile, the stage 2 samples ZXK-12-134 and ZXK-12-156 yield the $\Delta^{56}Fe_{pyrite-Mn-Fe\ carbonate}$ values of 0.82‰ and 0.78‰, respectively. If the mineral pairs are in Fe isotopic equilibrium, the $^{56}Fe/^{54}Fe$ fractionation factor $\alpha_{pyrite-Mn-Fe\ carbonate}$ is between 1.00032 and 1.00082. The $\Delta^{56}Fe_{pyrite-Mn-Fe\ carbonate}$ values of stage 2 samples both containing minor amounts of quartz are obviously higher than those of stage 1 samples. This is probably related to the Fe isotopic re-equilibrium caused by the second pulse overprint. This hypothesis is also evidenced by the fact that sample D52-3 cross-cut by quartz–boulangerite veins has higher $\Delta^{56}Fe_{pyrite-Mn-Fe\ carbonate}$ value than the other three samples from the same stage that have not been influenced by these later hydrothermal veins. Further research is needed to identify the $\alpha_{pyrite-Mn-Fe\ carbonate}$. The Mn–Fe carbonate, however, has lighter $\delta^{56}Fe$ values than the pyrite within a given mineral pair (Fig. 6A), which is consistent with the theory that iron carbonates are preferentially enriched in light Fe isotopes relative to pyrite (Wiesli et al., 2004; Polyakov and Soultanov, 2011; Wang and Zhu, 2012).

If all of these mineral pairs have attained Fe isotopic equilibrium then a fractionation factor can be used to estimate the temperature of formation as follows: $\Delta^{56}Fe_{pyrite-siderite} = \beta_1 X - \beta_2 \times 10^{-2} X^2 + \beta_3 \times 10^{-4} X^3$, where $X = 10^6/T^2$, T is temperature in K, and β_1, β_2, and β_3 are parameters (Polyakov and Mineev, 2000; Polyakov et al., 2007; Polyakov and Soultanov, 2011; Blanchard et al., 2009). The stage 1 and 2 mineral pairs yield temperatures of ~ 800 °C and ~500 °C, respectively, both of which are much higher than the homogenization temperatures of fluid inclusions trapped in stage 2 Mn–Fe carbonate and stage 3 quartz (230 °C–240 °C and 240 °C–270 °C, respectively; unpublished data). This can be explained by three possible reasons: (1) the mineral pairs have not attained Fe isotopic equilibrium; (2) the theoretical equation used here may not be suitable for these conditions; or (3) this equation is for pyrite and siderite mineral pairs whereas Mn–Fe carbonates form by the isomorphic substitution of Fe^{2+} and Mn^{2+} ions.

6.1.2. Zn isotope fractionation between Mn–Fe carbonate and sphalerite

Four Mn–Fe carbonate and sphalerite mineral pairs from the Zhaxikang deposit were analyzed in this study, although these data are insufficient to confirm whether the Mn–Fe carbonate and sphalerite have attained Zn isotopic equilibrium as per the $\delta^{66}Zn$–$\delta^{66}Zn$ diagram. The $\Delta^{66}Zn_{Mn-Fe\ carbonate-sphalerite}$ values for samples are 0.03‰ (stage 1; ZXK12-PD9-B2), −0.15‰ (stage 1; 14-9), 0.03‰ (stage 2; ZXK-12-34) and 0.04‰ (stage 2; ZXK-12-156), respectively. Three mineral pairs (samples ZXK12-PD9-B2, ZXK-12-34 and ZXK-12-156) contain sphalerite with lighter $\delta^{66}Zn$ values than the associated Mn–Fe carbonate (Fig. 6B). This is possible the result of Zn isotope equilibrium fractionation. In comparison, the other pair (sample 14-9) shows the reverse relationship, either because it did not reach Zn isotopic equilibrium (Fig. 6B) or it was modified after formation as the sample contain later minerals such as quartz, stibnite, and boulangerite (Fig. 5C4). These data suggest that sphalerite is generally preferentially enriched in light Zn isotopes relative to contemporaneously formed Mn–Fe carbonate and the $^{66}Zn/^{64}Zn$ fractionation factor $\alpha_{Mn-Fe\ carbonate-sphalerite}$ maybe around 1.00003–1.00004 although more data is needed.

6.2. Possible causes of isotopic variations

6.2.1. Fe isotopes

Previous research has identified several causes of Fe isotopic variations (Markl et al., 2006; Liu et al., 2014a, 2014b, 2014c), including kinetic fractionation resulting from disequilibrium chemical diffusion or thermal gradients (Richter et al., 2009; Huang et al., 2010; Teng et al., 2011), the different valence states of iron ions in precipitates and ore-forming hydrothermal systems (Johnson et al., 2002; Welch et al., 2003; Saunier et al., 2011; Wang and Zhu, 2012), kinetic Rayleigh fractionation (Butler et al., 2005; Wang et al., 2011; Syverson et al., 2013), and the mixing of multiple iron sources (Sun et al., 2013; Hou et al., 2014).

As the Fe^{3+} ions are preferentially enriched in heavy Fe isotopes relative to Fe^{2+} ions, the valence states of iron ions can influence Fe isotope fractionation between minerals and hydrothermal fluids with different valence states (i.e., ferrous and ferric minerals, Fe (II)aq and Fe (III)aq; Johnson et al., 2002; Welch et al., 2003; Wang and Zhu, 2012). However, the only iron-bearing minerals in the Zhaxikang deposit are Mn–Fe carbonate and pyrite, both of which contain Fe^{2+}, thereby eliminating the possibility that Fe isotopic variations were caused by the presence of iron ions with different valence states. The homogenization temperatures of fluid inclusions from Zhaxikang stage 2 Mn–Fe carbonate and stage 3 quartz are 230 °C–240 °C and 240 °C–270 °C, respectively (unpublished data). These low temperatures and thermal gradients indicate that kinetic fractionation would have had little influence on Fe isotope fractionation (Richter et al., 2009; Huang et al., 2010; Teng et al., 2011), in contrast to the significant Fe isotopic variation within samples from the Zhaxikang deposit. This suggests that the kinetic fractionation resulting from disequilibrium chemical diffusion or thermal gradients was also not the primary cause of the Fe isotopic variations recorded within these samples.

If all of the metals within the Zhaxikang deposit were derived from the same source, the kinetic Rayleigh fractionation of Fe

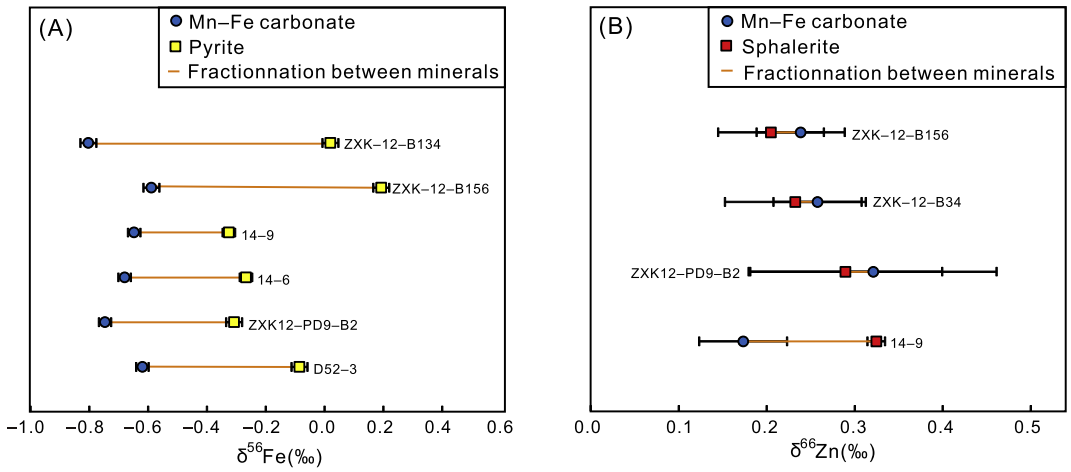

Fig. 6. (A) Diagram showing Fe isotope fractionation between Mn–Fe carbonate and pyrite mineral pairs. (B) Diagram showing Zn isotope fractionation between Mn–Fe carbonate and sphalerite mineral pairs.

isotopes in an open hydrothermal system could have caused Fe isotopic variations. For example, the δ^{56}Fe values of pyrite from different stages in the Xinqiao Cu–S–Fe–Au deposit gradually increase from earlier to later stages of mineralization (Wang et al., 2011). However, the δ^{56}Fe values of sulphides that formed during different stages of mineralization in the Xinqiao deposit generally overlap, yielding only small variations in δ^{56}Fe values between differing stages (Fig. 7; Wang et al., 2011; δ^{56}Fe values of stage 1 colloform pyrite: −0.83‰ to 0.10‰; stage 2 fine-grained pyrite: −0.71‰ to 0.37‰; stage 3 coarse-grained pyrite and chalcopyrite that formed almost simultaneously: −0.66‰ to 0.50‰). The Zhaxikang deposit shows similar results, with pyrite δ^{56}Fe values that gradually increase during the first three stages of mineralization (Fig. 7), from stage 1 (−0.33‰ to −0.09‰) through stage 2 (−0.30‰ to 0.19‰) to stage 3 (0.16‰ to 0.43‰). This suggests that kinetic Rayleigh fractionation is the main control on the Fe isotopic variations recorded within the deposit.

However, the second pulse of mineralization also probably modified the Fe isotopic compositions, as evidenced by the fact that the Fe isotopic compositions of pyrite are related to alteration during the second pulse of mineralization based on the observations of hand specimens and thin sections. The more significant the modification of these samples, the heavier the δ^{56}Fe values of the resulting pyrite, which indicates the overprint would make the δ^{56}Fe values heavier (Fig. 5A). Meanwhile, a stage 1 sample D52-3 (Fig. 4A) cross-cut by a later quartz–boulangerite vein displays heavier δ^{56}Fe value (−0.09‰) of pyrite than the other three samples (ZXK12-PD9-B2: −0.31‰, 14-6: −0.27‰ and 14-9: −0.33‰) from the same stage that have not been influenced by these later hydrothermal veins (Fig. 7). However, the Fe isotopic compositions of the Mn–Fe carbonates in the modified samples remain generally unchanged, primarily due to the larger volume of Mn–Fe carbonate relative to the amount of pyrite in these samples. This factor inhibited the modification of the compositions of these early-formed Mn–Fe carbonates. The pyrite within these modified samples also records clear evidence of recrystallization in the form of early formed fine-grained pyrite attaching to the crystal or growth planes of coarse-grained pyrite from stage 3 (Fig. 4Q). In addition, stage 3 sulphides contain lower Fe contents than those of the early formed sulphides (unpublished EPMA data) and the δ^{56}Fe values of stage 3 pyrite are heavier than those of pyrite from the first pulse of mineralization. These may be caused by two reasons: (1) the leaching of the second pulse of ore-forming fluid would preferentially take away parts of light Fe isotopes and the residual sulphides would have heavier δ^{56}Fe values

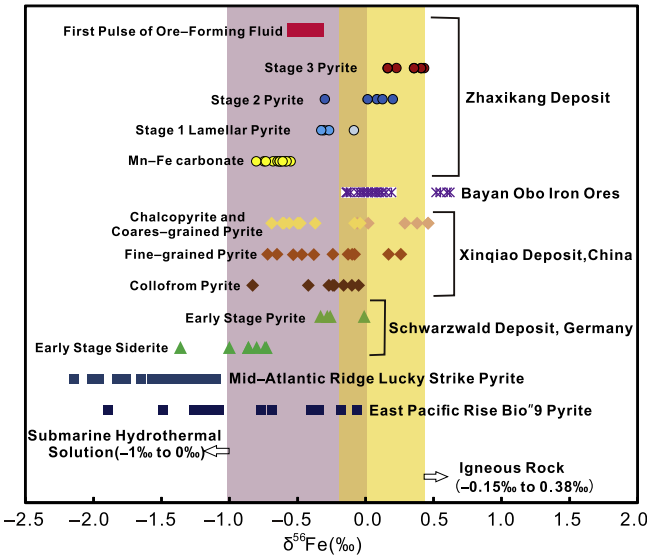

Fig. 7. Fe isotopic compositions of Mn–Fe carbonate and pyrite from different stages in the Zhaxikang deposit. Other Fe isotopic data for igneous rocks (Beard and Johnson, 1999; Zhu et al., 2002), submarine hydrothermal solutions (Sharam et al., 2001; Beard et al., 2003; Severmann et al., 2004; Rouxel et al., 2008; Bennett et al., 2009), the Mid-Atlantic Ridge Lucky Strike Pyrite (Rouxel et al., 2004), the East Pacific Rise Bio″9 Pyrite (Rouxel et al., 2008), the Schwarzwald hydrothermal vein deposit in Germany (Markl et al., 2006), the Xinqiao skarn deposit in China (Wang et al., 2011), and the Bayan Obo Fe-REE deposit in China (Sun et al., 2013) are also plotted for comparison.

(Markl et al., 2006; Wang et al., 2011). This hypothesis is also evidenced by the fact that the formation of stage 4 sulfosalt minerals need some Fe elements and the recrystallization of stage 3 pyrite (Fig. 4Q); (2) the ore-forming fluid of the second pulse of mineralization has heavier Fe isotopic compositions. As most of the stage 3 pyrite cut and replace earlier formed sulphides and Mn–Fe carbonates, the second reason maybe the main cause. All of the evidence suggest that the deposit was overprinted by the second pulse of mineralization that added to the Fe isotopic variations in the Zhaxikang deposit that were initially the result of kinetic Rayleigh fractionation.

6.2.2. Zn isotopes

The δ^{66}Zn values of the sphalerite in the Zhaxikang deposit vary from −0.03‰ to 0.35‰. Several possible causes of the Zn isotopic

variations have been identified by previous research, including temperature gradients (Mason et al., 2005; Toutain et al., 2008), kinetic Rayleigh fractionation (Kelley et al., 2009; Gagnevin et al., 2012), and the mixing of multiple zinc sources (Wilkinson et al., 2005). Toutain et al. (2008) identified large variations in the δ^{66}Zn values of fumarolic gases (0.05‰–0.85‰) and their condensates (1.48‰–1.68‰), suggesting that this fractionation was the result of a significant temperature gradient (297 °C–590 °C). However, other research suggests that lower temperature gradients (30 °C–50 °C) do not affect Zn isotopic compositions (Maréchal and Sheppard, 2002), with no correlation between δ^{66}Zn values and temperatures in the range of 60 °C–250 °C (Wilkinson et al., 2005). The homogenization temperatures of fluid inclusions from the Zhaxikang deposit described above suggest that the temperature gradients would have had a minimal effect on Zn isotopic variations.

ore-forming materials derived from a single source would be subjected to kinetic Rayleigh fractionation that would form ^{64}Zn-enriched sulphides during the early phases of the system as well as residual fluids and later precipitates with heavier δ^{66}Zn values, causing an increase in δ^{66}Zn values within precipitates over time (Archer et al., 2004; Mason et al., 2005; Wilkinson et al., 2005; John et al., 2008; Kelley et al., 2009; Wang and Zhu, 2010; Gagnevin et al., 2012). The δ^{66}Zn values of sphalerite in the Red Dog ore district in Alaska gradually increase from the early to late stages of deposit formation (stage 1: 0.01‰–0.21‰, stage 2: 0.04 ‰–0.25‰, stage 3: 0.06‰–0.30‰, and stage 4: 0.13‰–0.22‰), providing a typical example of kinetic Rayleigh fractionation (Kelley et al., 2009). However, the Zn isotopic variations of sphalerite in the Zhaxikang deposit yield a different pattern with δ^{66}Zn values that gradually decrease from the early to late stages of mineralization (Fig. 8B; stage 1: 0.16‰–0.35‰, stage 2: 0.09 ‰–0.23‰, and stage 3: −0.03‰ to 0.22‰). Therefore, we suggest that the overprint by the second pulse of mineralization caused the Zn isotopic variations that added to the variations resulting from kinetic Rayleigh fractionation. This is evidenced by the fact that the more significant modification the samples demonstrate, the lighter the δ^{66}Zn values of the sphalerite become (Fig. 5B), a similar relationship that is also recorded in the Fe isotopic compositions of pyrite within the deposit. This trend is also exemplified by a stage 1 sample D52-3 (Fig. 4A) that records modification by a later quartz–boulangerite vein and contains sphalerite with lighter δ^{66}Zn value (0.16‰) than the other three stage 1 samples (ZXK12-PD9-B2: 0.29‰, 14-6: 0.35‰ and 14-9: 0.32‰) that do not contain later hydrothermal veins (Fig. 8B). Meanwhile, the δ^{66}Zn value (0.17‰) of a Mn–Fe carbonate sample 14-9 (Fig. 5C4) that was overprinted by later minerals such as quartz, stibnite, and boulangerite is lighter than those of other unmodified or slightly modified Mn–Fe carbonate samples (Fig. 5C; ZXK12-PD9-B2: 0.32‰, ZXK-12-B156: 0.24‰ and ZXK-12-B34: 0.26‰). However, the laminae that hosts the sphalerite in this sample was not modified, meaning that the δ^{66}Zn value of the sphalerite in sample 14-9 remained unaffected. Slate samples cross-cut by quartz–pyrite veins (ZXK-11-31: 0.05‰ and PD6-50: 0.12‰) or overprinted by later-formed minerals such as stibnite and boulangerite (ZXK-11-17: 0.08‰) also have lighter δ^{66}Zn values, whereas a slate sample that was cross-cut by a stage 2 Mn–Fe carbonate–pyrite–sphalerite vein (ZXK-12-B17: 0.38‰) has heavier δ^{66}Zn value (Fig. 5D). Additionally, stage 3 sulphides have lower Zn concentrations than earlier formed sulphides (unpublished EPMA data) and the δ^{66}Zn values of sphalerite from the second pulse of mineralization are lighter than those of sphalerite from the first pulse of mineralization. There are two possible causes: (1) the ore-forming fluid of the second pulse of mineralization has lighter Zn isotopic compositions; (2) the leaching of the second pulse of ore-forming fluid could take away parts of the Zn with heavier Zn isotopes and make the δ^{66}Zn values of residual minerals becoming lighter. However, in view of that the main minerals of the second pulse of mineralization are Sb-bearing, which would has little influence on the δ^{66}Zn values due to the absent of Zn-bearing minerals, the second hypothesis is most possible the main cause. All of the evidence indicate that the Zn isotopic variations within the deposit are primary related to the overprint caused by the second pulse of mineralization.

6.3. Two pulses of mineralization and possible metal sources

6.3.1. Two pulses of mineralization

As mentioned above, the paragenesis of minerals during the first and second pulses of mineralization in the Zhaxikang deposit differ significantly. The early-formed sphalerite, pyrite and Mn–Fe carbonate record both recrystallization and remobilization

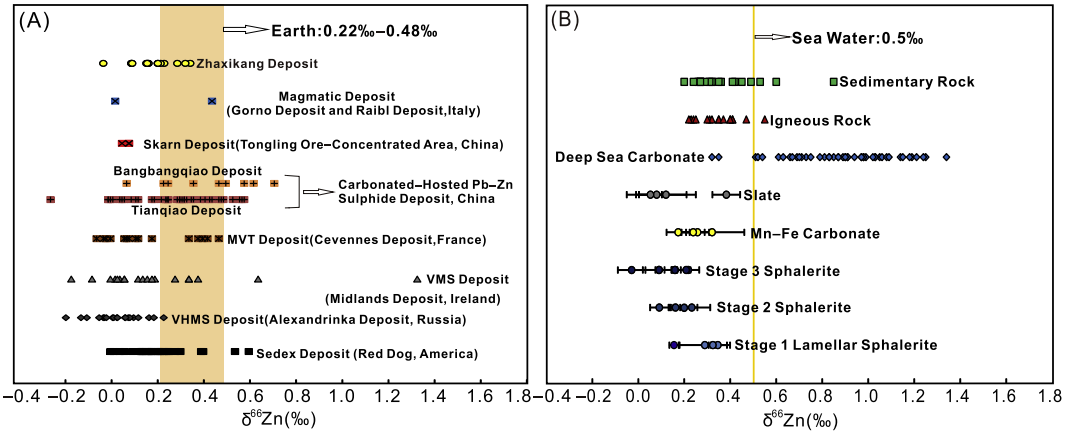

Fig. 8. (A) Zn isotopic compositions of sphalerite from the Zhaxikang deposit. Zn isotopic data for other deposits with different geneses, including the Red Dog SEDEX-type ore district in Alaska (Kelley et al., 2009), the Alexandrinka VHMS-type deposit in Russia (Mason et al., 2005), the Midlands VMS-type deposit in Ireland (Wilkinson et al., 2005), the Cévennes MVT-type deposit in France (Albarède, 2004), the skarn-type deposits in the Tongling ore-Concentrated Area in China (Wang and Zhu, 2010), the Gorno and Raibl magmatic-type deposit in Italy (Maréchal et al., 1999), and the Tianqiao and Bangbangqiao carbonated-hosted Pb–Zn sulphide deposits in China (Zhou et al., 2014), are also plotted for comparison. (B) Zn isotopic compositions of Mn–Fe carbonate, sphalerite from different stages, and slate from the Zhaxikang deposit compared with the compositions of sedimentary rocks (Maréchal et al., 2000; Weiss et al., 2007; Bentahila et al., 2008), igneous rocks (Viers et al., 2007; Bentahila et al., 2008; Toutain et al., 2008; Herzog et al., 2009), and deep-sea carbonates (Pichat et al., 2003). (For interpretation of the references to colour in this figure legend, the reader is referred to the web version of this article.)

(Fig. 4Q and D), which are evidenced by the presence of concentric annular sphalerite (Fig. 4G), different idiomorphic degrees of Mn–Fe carbonate (Fig. 4D), and the presence of Mn–Fe carbonate druse that contains idiomorphic columnar quartz, needle-like boulangerite, or valentinite formed by the oxidation of boulangerite during later stage hydrothermal activity (Fig. 5C4). Meanwhile, in view of the almost identical δ^{56}Fe values of Mn–Fe carbonates that formed during stages 1 and 2, the increasing δ^{56}Fe values and the decreasing δ^{66}Zn values as the samples showed higher degrees of modification (Fig. 5), the overprint by the second pulse of mineralization must the primary cause of the Fe–Zn isotopic variations within the Zhaxikang deposit. All of the evidence suggest that the Zhaxikang deposit records two pulses of mineralization, with stages 1 and 2 representing the first pulse that is dominated by the formation of Mn–Fe carbonates and sulphides, and stages 3–6 representing the second pulse that is dominated by the formation of quartz, calcite, sulfosalt minerals, and sulphides. In addition, the second pulse of mineralization partially modified the first pulse.

6.3.2. Possible metal sources

The Zhaxikang deposit has typical characteristics of hydrothermal origin deposits with moderate Fe isotopic variation range, relative light δ^{56}Fe values and distinct changes in δ^{56}Fe values across different stages of mineralization (Fig. 7). However, the sources of metal that formed during the two pulses of mineralization recorded in the deposit remain controversial. One possible source is the slate that hosts the deposit, with an unmodified slate sample (ZXK-12-B17: 0.38‰) yielding a δ^{66}Zn value that is similar to that expected for sedimentary rocks and is heavier than the δ^{66}Zn values of the sphalerite (Fig. 8B). However, any Zn derived from slate would yield sphalerite with heavier δ^{66}Zn values than the slate, as suggested by the continuous batch experimental research of Fernandez and Borrok (2009). Thus, the possibility that the metals is derived from slate can be eliminated.

As discussed in Section 6.1.1, the Mn–Fe carbonate and pyrite within the deposit may have been in Fe isotopic equilibrium. However, we do not know whether the Mn–Fe carbonate, the pyrite, and the hydrothermal fluid that formed the deposit have attained Fe isotopic equilibrium. If we assume that they were in Fe isotopic equilibrium, the following theoretical formulae can be used to calculate the Fe isotopic compositions of the ore-forming fluid:

$\Delta^{57}Fe_{pyrite-Fe(II)} = (0.946 \pm 0.0419)\,X - (6.7744 \pm 0.4279) \times 10^{-3}X^2 + (3.8254 \pm 0.5682) \times 10^{-5}X^3$ (where $X = 10^6/T^2$, T is in Kelvin; Polyakov and Mineev, 2000; Polyakov and Soultanov, 2011),

$\Delta^{56}Fe_{Fe(II)-siderite} = 0.48 \pm 0.22$‰ (Wiesli et al., 2004),

$\Delta^{x}Fe_{A-B} = \delta^{x}Fe_A - \delta^{x}Fe_B$ and $\Delta^{56}Fe = 0.678\Delta^{57}Fe$ (Wang and Zhu, 2012).

The δ^{56}Fe values of pyrite and Mn–Fe carbonate that formed during the first pulse of mineralization were used to independently calculate $\delta^{56}Fe_{Fe\ (II)}$ values, yielding δ^{56}Fe values from −1.28‰ to −0.34‰ and from −0.54‰ to 0.15‰, respectively. The fact that the pyrite and Mn–Fe carbonate that formed during the first pulse of mineralization were derived from the same source means that the overlap between these two sets of $\delta^{56}Fe_{Fe\ (II)}$ values (−0.54‰ to −0.34‰) is likely to represent the theoretical Fe isotopic compositional range of the first pulse of ore-forming fluid. This range overlaps with the δ^{56}Fe values of submarine hydrothermal solutions (−1‰ to 0‰; Fig. 7; Sharam et al., 2001; Beard et al., 2003; Severmann et al., 2004; Rouxel et al., 2008; Bennett et al., 2009). However, deuteric fluids exsolved from magmas may also be enriched in light Fe isotopes (Poitrasson and Freydier, 2005), although the processes that control Fe isotopic fractionation during fluid exsolution remain uncertain. Additionally, the Fe in hydrothermal fluids derived from igneous rocks is thought to be enriched in light Fe isotopes (Abe et al., 2008; Wang et al., 2011). All these indicate that the magmatic hydrothermal fluids may also have lighter δ^{56}Fe values than igneous rocks (−0.15‰ to 0.38‰; Fig. 7; Zhu et al., 2002). Therefore, we cannot be certain that the first pulse of mineralization was associated with either a submarine hydrothermal solution or a magmatic hydrothermal fluid. As mentioned in Section 6.2.1, the second pulse of mineralization has brought some Fe as we can see stage 3 pyrite cut and replace earlier sulphides (Fig. 4K). The Fe isotopic compositions of the second pulse of ore-bearing fluid must be heavier than those of the stage 3 pyrite (0.16‰–0.43‰), as ^{54}Fe-enriched sulphides preferentially form during the earlier periods of hydrothermal activity (Butler et al., 2005; Richter et al., 2009; Teng et al., 2011). Therefore, the Fe isotopic compositions of the second pulse of ore-bearing fluid was heavier than typical submarine hydrothermal solutions (Fig. 7), suggesting that the second pulse of mineralization may have been related to a magmatic hydrothermal fluid.

The δ^{66}Zn values of sphalerite in the Zhaxikang deposit range from −0.03‰ to 0.35‰ (Fig. 8B). Comparing with the δ^{66}Zn values of sphalerite from the Red Dog SEDEX-type ore district in Alaska (0‰–0.6‰; Kelley et al., 2009), the Alexandrinka VHMS-type deposit in Russia (−0.20‰ to 0.23‰; Mason et al., 2005), the Midlands VMS-type deposit in Ireland (−0.17‰ to 1.33‰; Wilkinson et al., 2005), the Cévennes Mississippi Valley Type (MVT) deposit in France (−0.06‰ to 0.47‰; Albarède, 2004), the skarn deposits of the Tongling ore field in Anhui Province, China (0.05‰–0.08‰; Wang and Zhu, 2010), the Gorno and Raibl magmatic-type deposits in Italy (0.02‰–0.44‰; Maréchal et al., 1999), and the Tianqiao (−0.26‰ to 0.58‰) and Bangbangqiao (0.07‰ to 0.71‰) carbonate-hosted Pb–Zn sulphide deposits in China (Zhou et al., 2014; Fig. 8A), there are large overlaps in the Zn isotopic variation range of these deposits with different geneses (Fig. 8A). Meanwhile, in view of the Zn isotope fractionation that occurs during fluid evolution and sulphide precipitation, it is difficult to make sure the first pulse of mineralization was associated with either a submarine hydrothermal solution or a magmatic hydrothermal fluid.

Overall, our research demonstrates that Fe–Zn isotopes have the potential to trace the sources of metal within mineral deposits and provide insights into ore-forming processes, although more work is required to further constrain the origin of the Zhaxikang Sb–Pb–Zn–Ag deposit.

7. Conclusions

1. In the Zhaxikang deposit, pyrite is preferentially enriched in heavy Fe isotopes relative to cogenetic Mn–Fe carbonates, whereas sphalerite is preferentially enriched in light Zn isotopes relative to cogenetic Mn–Fe carbonate.
2. The Fe–Zn isotopic variations within the Zhaxikang deposit are the result of kinetic Rayleigh fractionation and overprint caused by the second pulse of mineralization.
3. The second pulse of mineralization has brought some Fe and taken away parts of Zn. The overprint by the second pulse of mineralization causes the lighter δ^{66}Zn values and heavier δ^{56}Fe values of modified samples.
4. The Fe–Zn isotopes demonstrated the presence of two pulses of mineralization in the Zhaxikang deposit, with the first pulse comprising stages 1 and 2, and the second pulse comprising stages 3–6. The Fe isotopic data presented here suggest that the second pulse was likely related to a magmatic hydrothermal fluid. However, further work is needed to constrain the metal source of first pulse of mineralization in Zhaxikang deposit.

Conflict of interest

We declare that we do not have any commercial or associative interest that represents a conflict of interest in connection with the submitted work.

Acknowledgments

We would like to express our gratitude to two anonymous reviewers and Prof. Franco Pirajno for their constructive comments and suggestions. Dr. Sheng–Ao Liu and Yongsheng He are also thanked for helpful discussions and revision advices, which have largely improved this manuscript. This research was supported by the Program for Changjiang Scholars and Innovative University Research Teams (IRT14R54, IRT1083), National Key Project for Basic Research of China (2015CB452600), the Fundamental Research Funds for the Central Universities (2652015044 and 2652015354), and Beijing Higher Education Young Elite Teacher Project.

References

Abe, H., Ina, K., Kitamura, H., Sumiyoshi, H., Tatsukawa, S., Yoshioka, H., Fujikura, Y., 2008. The role of volatile exsolution and sub-solidus fluid/rock interactions in producing high $^{56}Fe/^{54}Fe$ ratios in siliceous igneous rocks. Geochim. Cosmochim. Acta 72, 4379–4396.

Albarède, F., 2004. The stable isotope geochemistry of copper and zinc. Rev. Mineral. Geochem. 55, 409–427.

Archer, C., Vance, D., Butler, I., 2004. Abiotic Zn isotope fractionations associated with ZnS precipitation. 14th Annual V M Goldschmidt Conference. Geochim. Cosmochim. Acta 68, A325.

Armijo, R., Tapponnier, P., Mercier, J.L., Han, T.L., 1986. Quaternary extension in southern Tibet: field observations and tectonic implications. J. Geophy. Res. 91, 13803–13872.

Beard, B.L., Johnson, C.M., 1999. High precision iron isotope measurements of terrestrial and lunar materials. Geochim. Cosmochim. Acta 63, 1653–1660.

Beard, B.L., Johnson, C.M., Von Damm, K.L., Poulson, R.L., 2003. Iron isotope constraints on Fe cycling and mass balance in oxygenated earth oceans. Geology 31, 629–632.

Belshaw, N.S., Zhu, X.K., Guo, Y., O'Nions, R.K., 2000. High precision measurement of iron isotopes by plasma source mass spectrometry. Int. J. Mass Spectrom. 197, 191–195.

Bennett, S.A., Rouxel, O., Schmidt, K., Garbe-Schoznberg, D., Statham, P.J., German, C. R., 2009. Iron isotope fractionation in a buoyant hydrothermal plume, 5 S Mid-Atlantic Ridge. Geochim. Cosmochim. Acta 73, 5619–5634.

Bentahila, Y., Othman, D.B., Luck, J.M., 2008. Strontium, lead and zinc isotopes in marine cores as tracers of sedimentary provenance: a case study around Taiwan orogen. Chem. Geol. 248, 62–82.

Blanchard, M., Poitrasson, F., Méheut, M., Lazzeri, M., Mauri, F., Balan, E., 2009. Iron isotope fractionation between pyrite (FeS_2), hematite (Fe_2O_3) and siderite ($FeCO_3$): a first-principles density functional theory study. Geochim. Cosmochim. Acta 73, 6565–6578.

Blisniuk, P.M., Hacker, B.R., Glodny, J., Ratschbacher, L., Bi, S.W., Wu, Z.H., McWilliams, M.O., Calvert, A., 2001. Normal faulting in central Tibet since at least 13.5Myr ago. Nature 412, 628–632.

Butler, I.B., Archer, C., Vance, D., Oldroyd, A., Rickard, D., 2005. Fe isotope fractionation on FeS formation in ambient aqueous solution. Earth Planet. Sci. Lett. 236, 430–442.

Chen, Y., Pirajno, F., Sui, Y., 2005. Geology and D-O-C isotope systematics of the Tieluping silver deposit, Henan, China: implications for ore genesis. Acta. Geo. Sin. 79, 106–119.

Cheng, Y., Mao, J., Zhu, X., Wang, Y., 2013. Iron isotope fractionation during supergene weathering process and its application to constrain ore genesis in Gaosong deposit, Gejiu district. SW China. Gondwana Res. 27, 1283–1291.

England, P., Houseman, G., 1989. Extension during continental convergence, with application to the Tibetan Plateau. J. Geophy. Res. 94, 17561–17579.

Fernandez, A., Borrok, D.M., 2009. Fractionation of Cu, Fe, and Zn isotopes during the oxidative weathering of sulfide-rich rocks. Chem. Geol. 264, 1–12.

Gagnevin, D., Boyce, A.J., Barrie, C.D., Menuge, J.F., Blakeman, R.J., 2012. Zn, Fe and S isotope fractionation in a large hydrothermal system. Geochim. Cosmochim. Acta 88, 183–198.

Garzanti, E., 1999. Stratigraphy and sedimentary history of the Nepal Tethys Himalaya passive margin. J. Asian Earth Sci. 17, 805–827.

Graham, S., Pearson, N., Jackson, S., Griffin, W., O'reilly, S.Y., 2004. Tracing Cu and Fe from source to porphyry: in situ determination of Cu and Fe isotope ratios in sulfides from the Grasberg Cu–Au deposit. Chem. Geol. 207, 147–169.

Harrison, T.M., Copeland, P., Kidd, W.S.F., Yin, A., 1992. Raising Tibet. Science 255, 1663–1670.

He, Y.S., Ke, S., Teng, F.Z., Wang, T.T., Wu, H.J., Lu, Y.H., Li, S.G., 2015. High-Precision iron isotope analysis of geological reference materials by High-Resolution MC-ICP-MS. Geostand. Geoanal. Res. 39, 341–356.

Herzog, G.F., Moynier, F., Albarède, F., Berezhnoy, A.A., 2009. Isotopic and elemental abundances of copper and zinc in lunar samples, zagami, pele's hairs, and a terrestrial basalt. Geochim. Cosmochim. Acta 73, 5884–5904.

Hou, K., Li, Y., Gao, J., Liu, F., Qin, Y., 2014. Geochemistry and Si–O–Fe isotope constraints on the origin of banded iron formations of the Yuanjiacun Formation, Lvliang Group, Shanxi. China. Ore Geol. Rev. 57, 288–298.

Huang, F., Chakraborty, P., Lundstrom, C.C., Holmden, C., Glessner, J.J.G., Kieffer, S. W., Lesher, C.E., 2010. Isotope fractionation in silicate melts by thermal diffusion. Nature 464, 396–400.

Huang, X.W., Qi, L., Meng, Y.M., Chen, D., Ling, H.D., 2015. Origin of siderite mineralization in western Guizhou, SW China: constrains from REES, C, O, Sr and S isotopes. Ore Geol. Rev. 66, 252–265.

Icopini, G.A., Anbar, A.D., Ruebush, S.S., Tien, M., Brantley, S.L., 2004. Iron isotope fractionation during microbial reduction of iron: the importance of adsorption. Geology 32, 205–208.

Jeffrey, L., Hacker, B.R., Dinklage, W.S., Yu, W., Phillip, G., Andrew, C., Wang, J.L., Chen, W.J., Ann, E.B., William, M., 2000. Evolution of the Kangmar dome, southern Tibet: structural, petrologic, and thermochronologic constraints. Tectonics 19, 872–895.

John, S.G., Rouxel, O.J., Craddock, P.R., Engwall, A.M., Boyle, E.A., 2008. Zinc stable isotopes in seafloor hydrothermal vent fluids and chimneys. Earth Planet. Sci. Lett. 269, 17–28.

Johnson, C.M., Skulan, J.L., Beard, B.L., Sun, H., Nealson, K.H., Braterman, P.S., 2002. Isotopic fractionation between Fe (III) and Fe (II) in aqueous solutions. Earth Planet. Sci. Lett. 195, 141–153.

Kelley, K.D., Wilkinson, J.J., Chapman, J.B., Crowther, H.L., Weiss, D.J., 2009. Zinc isotopes in sphalerite from base metal deposits in the red dog district, northern Alaska. Econ. Geol. 104, 767–773.

Lefort, P., 1975. Himalayas-collided range-present knowledge of continental arc. Am. J. Sci. A275, l–44.

Lefort, P., Yin, A., Harrison, T.M., 1996. Evolution of the Himalaya. The tectonics of Asia. Cambridge University Press, New York, pp. 95–106.

Liang, W., Hou, Z.Q., Yang, Z.S., Li, Z.Q., Huang, K.X., Zhang, S., Li, W., Zheng, Y.C., 2013. Remobilization and overprinting in the Zhaxikang Pb-Zn-Ag-Sb polymetal ore deposit, Southern Tibet: implications for its metallogenesis. Acta. Petrol. Sin. 29, 3828–3842 (In Chinese with English abstract).

Liang, W., Zheng, Y.C., Yang, Z.S., Li, Z.Q., Liu, Y.C., Liu, Y.F., Li, Q.G., Sun, Z.Q., Fu, Q., Hou, Z.Q., 2014. Multiphase and polystage metallogenic process of the Zhaxikang large-size Pb-Zn-Ag-Sb polymetallic deposit in Southern Tibet and its implications. Acta. Petrol. Miner. 33, 64–78 (In Chinese with English abstract).

Li, D.D., Liu, S.A., Li, S., Li, D., Liu, S.A., 2015. Copper isotope fractionation during adsorption onto kaolinite: experimental approach and applications. Chem. Geol. 396, 74–82.

Li, G.Q., Gu, X.X., Cheng, W.B., Zhang, Y.M., Zhang, Y., Dai, H.Z., Lv, P.R., Zhang, X.G., Xia, B.B., 2014. The analysis of metallogenic material sources of the Zhaxikang antimony (sulfur salts) polymetallic deposits in southern Tibet: concurrent discussion on the differences of the ore sources of major mineral deposits in north Himalayan metallogenic belt. Earth Sci. Frontiers 21, 90–104 (In Chinese with English abstract).

Li, Z.Q., Hou, Z., Nie, F., 2005. Characteristic and distribution of the partial melting layers in the upper crust: evidence from active hydrothermal fluid in the south Tibet. Acta Geol. Sin. 79, 69–77 (In Chinese with English abstract).

Lin, B., Tang, J.X., Zheng, W.B., Leng, Q.F., Yang, C., Tang, X.Q., Hang, Y., Wang, Y.Y., Tan, J.Y., 2014. Petrochemical features, zircon U-Pb dating and Hf isotopic composition of the rhyolite in Zhaxikang deposit, Southern Xizang (Tibet). Geol. Rev. 60, 178–189 (In Chinese with English abstract).

Liu, G., Einsele, G., 1994. Sedimentary history of the Tethyan basin in the Tibetan Himalayas. Geol. Rundsch. 82, 32–61.

Liu, P.P., Zhou, M.F., Luais, B., Cividini, D., Rollion-Bard, C., 2014a. Disequilibrium iron isotopic fractionation during the high-temperature magmatic differentiation of the Baima Fe–Ti oxide-bearing mafic intrusion. SW China. Earth Planet. Sci. Lett. 399, 21–29.

Liu, S.A., Li, D.D., Li, S.G., Teng, F.Z., Ke, S., He, Y.S., Lu, Y.H., 2014b. High-precision copper and iron isotope analysis of igneous rock standards by MC-ICP-MS. J. Anal. At. Spectrom. 29, 122–133.

Liu, S.A., Teng, F.Z., Li, S., Wei, G.J., Ma, J.L., Li, D.D., 2014c. Copper and iron isotope fractionation during weathering and pedogenesis: insights from saprolite profiles. Geochim. Cosmochim. Acta 146, 59–75.

Liu, S.A., Wang, Z.Z., Li, S.G., Huang, J., Yang, W., 2016. Zinc isotope evidence for a large-scale carbonated mantle beneath eastern China. Earth Planet. Sci. Lett. 444, 169–178.

Lv, Y.W., Liu, S.A., Zhu, J.M., Li, S.G., 2015. Copper and zinc isotope fractionation during deposition and weathering of highly metalliferous black shales in central China. Chem. Geol. 422, 82–93.

Mao, J.W., Zhang, Z.H., Wang, Y.T., Jia, Y.F., Robert, K., 2003. Nitrogen isotope and content record of mesozoic orogenic gold deposits surrounding the North China craton. Sci. China Ser. D. 46, 231–245.

Maréchal, C.N., Télouk, P., Albarède, F., 1999. Precise analysis of copper and zinc isotopic compositions by plasma-source mass spectrometry. Chem. Geol. 156, 251–273.

Maréchal, C.N., Emmanuel, N., Chantal, D., Francis, A., 2000. Abundance of zinc isotopes as a marine biogeochemical tracer. Geochem. Geophy. Geosyst 1. 1999GC–000029.

Maréchal, C.N., Sheppard, S.M.F., 2002. Isotopic fractionation of Cu and Zn between chloride and nitrate solutions and malachite or smithsonite at 30 °C and 50 °C. Geochim. Cosmochim. Acta 66, A484.
Markl, G., Wagner, T., Blanckenburg, F.V., 2006. Iron isotope fractionation during hydrothermal ore deposition and alteration. Geochim. Cosmochim. Acta 70, 3011–3030.
Mason, T.F.D., Weiss, D.J., Chapman, J.B., Wilkinson, J.J., Tessalina, S.G., Spiro, B., Horstwood, M.S.A., Spratt, J., Coles, B.J., 2005. Zn and Cu isotopic variability in the Alexandrinka volcanic-hosted massive sulphide (VHMS) ore deposit, Urals. Russia. Chem. Geol. 221, 170–187.
Meng, X.J., Yang, Z.S., Qi, X.X., Hou, Z.Q., Li, Z.Q., 2008. Silicon-oxygen-hydrogen isotopic compositions of Zhaxikang antimony polymetallic deposit in Southern Tibet and its responses to the ore-controlling structure. Acta. Petrol. Sin. 24, 1649–1655 (In Chinese with English abstract).
Molnar, P., Tapponnier, P., 1978. Activetectonics of Tibet. J. Geophy. Res. 83, 5361–5375.
Murphy, M.A., Yin, A., Kapp, P., Harrison, T.M., Manning, C.E., Ryerson, F.J., et al., 2002. Structural evolution of the Gurla Mandhata detachment system, southwest Tibet. Geol. Soc. Am. Bull. 114, 428–447.
Nie, F.J., Hu, P., Jiang, S.H., Li, Z.Q., Liu, Y., 2005. Type and temporal-spatial distribution of gold and antimony deposits (prospects) in Southern Tibet. China. Acta Geol. Sin. 79, 374–384 (In Chinese with English abstract).
Pan, Y., Kidd, W.S.F., 1992. Nyainqentanglha shear zone: A Late Miocene extensional detachment in the southern Tibetan Plateau. Geology 20, 75–778.
Pan, G.T., Wang, L.Q., Zhu, D.C., 2004. Thoughts on some important scientific problems in regional geological survey of the Qinghai-Tibet plateau. Regional Geol. China 23, 12–19 (In Chinese with English abstract).
Pan, G.T., Mo, X.X., Hou, Z.Q., Zhu, D.C., Wang, L.Q., Li, G.M., Zhao, Z.D., Geng, Q.R., Liao, Z.L., 2006. Spatial-temporal framework of the Gangdese Orogenic Belt and its evolution. Acta Petrol. Sin. 22, 521–533 (In Chinese with English abstract).
Pichat, S., Douchet, C., Albarède, F., 2003. Zinc isotope variations in deep-sea carbonates from the eastern equatorial Pacific over the last 175 ka. Earth Planet. Sci. Lett. 210, 167–178.
Poitrasson, F., Freydier, R., 2005. Heavy iron isotope composition of granites determined by high resolution MC-ICP-MS. Chem. Geol. 222, 132–147.
Polyakov, V.B., Mineev, S.D., 2000. The use of Mössbauer spectroscopy in stable isotope geochemistry. Geochim. Cosmochim. Acta 64, 849–865.
Polyakov, V.B., Clayton, R.N., Horita, J., Mineev, S.D., 2007. Equilibrium iron isotope fractionation factors of minerals: reevaluation from the data of nuclear inelastic resonant X-ray scattering and Mössbauer spectroscopy. Geochim. Cosmochim. Acta 71, 3833–3846.
Polyakov, V.B., Soultanov, D.M., 2011. New data on equilibrium iron isotope fractionation among sulfides: Constraints on mechanisms of sulfide formation in hydrothermal and igneous systems. Geochim. Cosmochim. Acta 75, 1957–1974.
Richter, F.M., Dauphas, N., Teng, F.Z., 2009. Non-traditional fractionation of non-traditional isotopes: evaporation, chemical diffusion and Soret diffusion. Chem. Geol. 258, 92–103.
Rouxel, O., Fouquet, Y., Ludden, J.N., 2004. Subsurface processes at the lucky strike hydrothermal field, Mid-Atlantic Ridge: evidence from sulfur, selenium, and iron isotopes. Geochim. Cosmochim. Acta 68, 2295–2311.
Rouxel, O., Iii, W.C.S., Bach, W., Edwards, K.J., 2008. Integrated Fe- and S-isotope study of seafloor hydrothermal vents at East Pacific Rise 9–10 N. Chem. Geol. 252, 214–227.
Saunier, G., Pokrovski, G.S., Poitrasson, F., 2011. First experimental determination of iron isotope fractionation between hematite and aqueous solution at hydrothermal conditions. Geochim. Cosmochim. Acta 75, 6629–6654.
Searle, M.P., 1999. Emplacement of Himalayan leucogranites by magma Injection along giant sill complexes: Examples from the Cho Oyu, Gyachung Kang and Everest leucogranites (Nepal Himalaya). J. Asian Earth Sci. 17, 773–783.
Severmann, S., Johnson, C.M., Beard, B.L., German, C.R., Edmonds, H.N., Chiba, H., Green, D.R.H., 2004. The effect of plume processes on the Fe isotope composition of hydrothermally derived Fe in the deep ocean as inferred from the rainbow vent site, Mid-Atlantic ridge, 36 14′N. Earth Planet. Sci. Lett. 225 (1), 63–76.
Sharam, M., Polizzotto, M., Anbar, A.D., 2001. Iron isotopes in hot springs along the Juan de Fuca Ridge. Earth Planet. Sci. Lett. 194, 39–51.
Spratt, J.E., Jones, A.G., Nelson, K.D., 2005. Crustal structure of the India-Asia collision zone, southern Tibet, from Indepth Mt investigations. Phys. Earth Planet. Interiors 150, 227–237.
Sun, J., Zhu, X.K., Chen, Y.L., Fang, N., 2012. Fe isotope compositions of related geological formation in Bayan Obo area and their constrains on the genesis of Bayan Obo ore deposit. Acta Geol. Sin. 86, 819–828 (In Chinese with English abstract).
Sun, J., Zhu, X.K., Chen, Y.L., Fang, N., 2013. Iron isotopic constraints on the genesis of Bayan Obo ore deposit, Inner Mongolia. China. Precambrian Res. 235, 88–106.
Syverson, D.D., Borrok, D.M., Seyfried, W.E., 2013. Experimental determination of equilibrium Fe isotopic fractionation between pyrite and dissolved Fe under hydrothermal conditions. Geochim. Cosmochim. Acta 122, 170–183.
Taylor, H.P., 1974. The application of oxygen and hydrogen isotope studies to problems of hydrothermal alteration and ore deposition. Econ. Geol. 69, 843–883.
Teng, F.Z., Dauphas, N., Helz, R.T., Gao, S., Huang, S., 2011. Diffusion-driven magnesium and iron isotope fractionation in Hawaiian olivine. Earth Planet. Sci. Lett. 308, 317–324.
Toutain, J.P., Sonke, J., Munoz, M., Nonell, A., Polvé, M., Viers, J., Freydier, R., Sortino, F., Joron, J.L., Sumarti, S., 2008. Evidence for Zn isotopic fractionation at Merapi volcano. Chem. Geol. 253, 74–82.
Viers, J., Oliva, P., Nonell, A., Gélabert, A., Sonke, J.E., Freydier, R., Gainvilleet, R., Dupré, B., 2007. Evidence of Zn isotopic fractionation in a soil-plant system of a pristine tropical watershed (Nsimi, Cameroon). Chem. Geo. 239, 124–137.
Visonà, D., Lombardo, B., 2002. Two-mica and tourmaline leucogranites from the Everest-Makalu region (Nepal-Tibet). Himalayan leucogranite genesis by isobaric heating? Lithos 62, 125–150.
Wang, S.X., Zhu, X.K., Song, X.Y., Chen, L.M., 2012a. Fe Isotopic Characteristics of V-Ti Magnetite Deposit in Panzhihua Area of Sichuan Province and Their Genetic Implications. Acta Geosci. Sin. 33, 995–1004 (In Chinese with English abstract).
Wang, Y.Y., Tang, J.X., Zheng, W.B., Lin, B., Leng, Q.F., Chen, W., 2012b. A tentative discussion on ore fabric and genesis of the Zhaxikang Zn-polymetallic deposit, Lhunze County, Tibet. Acta Geosci. Sin. 33, 681–692 (In Chinese with English abstract).
Wang, Y., Zhu, X.K., 2010. Application of Zn isotopes to study of mineral deposits: a review. Mineral Deposits 29, 843–852 (In Chinese with English abstract).
Wang, Y., Zhu, X.K., Mao, J.W., Li, Z.H., Cheng, Y.B., 2011. Iron isotope fractionation during skarn-type metallogeny: a case study of Xinqiao Cu–S–Fe–Au deposit in the Middle-Lower Yangtze valley. Ore Geol. Rev. 43, 194–202.
Wang, Y., Zhu, X.K., 2012. Fe isotope systematics and its implications in ore deposit geology. Acta Petrol. Sin. 28, 3638–3654 (In Chinese with English abstract).
Welch, S.A., Beard, B.L., Johnson, C.M., Braterman, P.S., 2003. Kinetic and equilibrium Fe isotope fractionation between aqueous Fe (II) and Fe (III). Geochim. Cosmochim. Acta 67, 4231–4250.
Weiss, D.J., Rausch, N., Mason, T.F.D., Coles, B.J., Wilkinson, J.J., Ukonmaanaho, L., Arnold, T., Nieminen, T.M., 2007. Atmospheric deposition and isotope biogeochemistry of zinc in ombrotrophic peat. Geochim. Cosmochim. Acta 71, 3498–3517.
Wiesli, R.A., Beard, B.L., Johnson, C.M., 2004. Experimental determination of Fe isotope fractionation between aqueous Fe(II), siderite and "green rust" in abiotic systems. Chem. Geol. 211, 343–362.
Wilkinson, J.J., Weiss, D.J., Mason, T.F.D., Coles, B.J., 2005. Zinc isotope variation in hydrothermal systems: preliminary evidence from the Irish Midlands ore field. Econ. Geol. 100, 583–590.
Williams, H., Turner, S., Kelley, S., Harris, N., 2001. Age and composition of dikes in southern Tibet: New constraints on the timing of east-west extension and its relationship to postcollisional volcanism. Geology 29, 339–342.
Yan, B., Zhu, X.K., Tang, S.H., Zhu, M.Y., 2010. Fe isotopic characteristics of the Neoproterozoic BIF in Guangxi Province and its implications. Acta Geol. Sin. 84, 1080–1086 (In Chinese with English abstract).
Yeh, H.W., Hein, J.R., Ye, J., Fan, D., 1999. Stable isotope, chemical, and mineral compositions of the middle Proterozoic Lijiaying Mn deposit, Shaanxi Province, China. Ore Geol. Rev. 15, 55–69.
Yin, A., Kapp, P.A., Murphy, M.A., Manning, C.E., Harrison, M.H., Grove, M., Lin, D., Deng, X.G., Wu, C.M., 1999. Significant Late Neogene east-west extension in northern Tibet. Geology 27, 787–790.
Yin, A., 2000. Mode of Cenozoic east-west extension in Tibet suggesting common origin of rifts in Asia during the Indo-Asian collision. J. Geophy. Res. 105, 21745–21759.
Yin, A., Harrison, T.M., 2000. Geologic evolution of the Himalayan-Tibetan orogeny. Annu. Rev. Earth Planet. Sci. 28, 211–280.
Yu, G.M., Wang, C.S., 1990. Sedimentary Geology of Tethys, Tibet. Geology Publishing House, Beijing (In Chinese).
Zeng, L.S., Liu, J., Gao, L.E., 2009. Early oligocene anatexis in the yardoi gneiss dome, southern Tibet and geological implications. Sci. Bull. 54, 104–112 (In Chinese with English abstract).
Zeng, L.S., Gao, L.E., Dong, C., Tang, S., 2012. High-pressure melting of metapelite and the formation of Ca-rich granitic melts in the Namche Barwa massif, southern Tibet. Gondwana Res. 21, 138–151.
Zhang, G.Y., Zheng, Y.Y., Zhang, J.F., 2011. Ore-control structural and geochronologic constrain in shalagang antimony deposit in southern Tibet, China. Acta Petrol. Sin. 27, 2143–2149 (In Chinese with English abstract).
Zhang, H.F., Gao, S., 2005. Geochemistry. Geology Publishing House, Beijing (In Chinese).
Zhang, J.F., Zheng, Y.Y., Zhang, G.Y., Gao, S.B., Ye, X.R., Zhang, Z., Liu, M.Y., Li, J.Q., 2010. Genesis of Zhaxikang Pb-Zn-Sb-Ag deposit in northern Himalaya: constraints from multi-isotope geochemistry. Earth Sci. 35, 1000–1010 (In Chinese with English abstract).
Zhang, S.K., 2013. Geology and geochemistry characteristics of Zhaxikang antimony polymetallic deposits, southern Tibet. Master Graduate Dissertation. China University of Geoscience, Beijing. Chapter 4 and 5, 47–99 (In Chinese).
Zheng, Y.Y., Liu, M.Y., Sun, X., Yuan, E.H., Tian, L.M., Zheng, H.T., Zhang, G.Y., Zhang, L. H., 2012. Type, discovery process and significance of Zhaxikang antimony polymetallic ore deposit. Tibet. Earth Sci. 37, 1004–1014 (In Chinese with English abstract).
Zheng, Y.Y., Sun, X., Tian, L.M., Zheng, H.T., Miao, Y., Yang, W.T., Zhou, T.C., Geng, X. B., 2014. Mineralization, deposit type and metallogenic age of the gold antimony polymetallic belt in the eastern part of north Himalayan. Geotecton. Metall. 38, 108–118 (In Chinese with English abstract).
Zheng, Y.Y., Sun, X., Gao, S.B., Xu, R.K., Tian, L.M., Zheng, H.T., Zheng, L., Xia, S.L., Li, M., Geng, X.B., Wang, D., Wu, S., Liu, Q.Q., Song, Q.J., 2016. Target optimization and demonstrate research of Au-Sb Polymetallic Metallogenic Belt in Southern Tibet. Project Report. China University of Geoscience, Wuhan. Chapter 4, 66–98 (In Chinese).

Zhou, J.X., Huang, Z.L., Zhou, M.F., Zhu, X.K., Muchez, P., 2014. Zinc, sulfur and lead isotopic variations in carbonate-hosted Pb–Zn sulfide deposits, southwest China. Ore Geol. Rev. 58, 41–54.

Zhu, B., Zhang, H.F., Zhao, X.M., He, Y.S., 2016. Iron isotope fractionation during skarn-type alteration: implications for metal source in the Han-Xing iron skarn deposit. Ore Geol. Rev. 74, 139–150.

Zhu, D.C., Chung, S.L., Mo, X.X., Zhao, Z.D., Niu, Y.L., Song, B., Yang, Y.H., 2009. The 132 Ma Comei-Bunbury large igneous province: Remnants identified in present-day southeastern Tibet and southwestern Australia. Geology 37, 583–586.

Zhu, D.C., Zhao, Z.D., Niu, Y.L., Mo, X.X., Chung, S.L., Hou, Z.Q., Wang, L.Q., Wu, F.Y., 2011. The Lhasa terrane, record of a microcontinent and its histories of drift and growth. Earth Planet. Sci. Lett. 301, 241–255.

Zhu, L.K., Gu, X.X., Li, G.Q., Zhang, Y.M., Cheng, W.B., Bian, X.D., 2012. Fluid inclusions in the Zhaxikang Pb-Zn-Sb polymetallic deposit, south Tibet, and its geological significance. Geoscience 26, 453–643 (In Chinese with English abstract).

Zhu, X.K., Guo, Y., Williams, R.J.P., O'Nions, R.K., Matthews, A., Belshaw, N.S., 2002. Mass fractionation processes of transition metal isotopes. Earth Planet. Sci. Lett. 200, 47–62.

Zhu, X.K., Li, Z.H., Zhao, X.M., Tang, S.H., Li, Y.H., 2008. Fe isotope characteristics of early Precambrian pyrite deposits and their geological significance: examples from Shandong and Hebei Provinces. Acta. Petrol. Miner. 27, 429–434 (In Chinese with English abstract).